

Contents lists available at ScienceDirect

Acta Materialia

journal homepage: www.elsevier.com/locate/actamat



Overview article

Effects of microstructure and composition on constitutive response of high temperature shape memory alloys: Micromechanical modeling using 3-D reconstructions with experimental validation



Jobin K. Joy^a, Tejas Umale^b, Dexin Zhao^b, Alexandros Solomou^a, Kelvin Xie^b, Ibrahim Karaman^b, Dimitris C. Lagoudas^{a,b,*}

- ^a Department of Aerospace Engineering, Texas A&M University, College Station, TX 77843, United States
- ^b Department of Materials Science and Engineering, Texas A&M University, College Station, TX 77843, United States

ARTICLE INFO

Article history: Received 3 December 2021 Revised 26 March 2022 Accepted 5 April 2022 Available online 8 April 2022

Keywords: NiTiHf Shape memory alloys Precipitation hardening Micromechanics Finite element analysis TEM microstructure

ABSTRACT

NiTiHf alloys are high temperature Shape Memory Alloys (SMAs) suitable for actuation applications in a wide range of temperatures. Aging heat treatments in NiTiHf SMAs cause the formation of nano-sized, non-transforming and elastic precipitates, which modify phase transformation behavior. Experimental observations of the aged alloys showed a counterintuitive trend of increasing phase transformation strain with precipitation. In order to predict such microstructure effects on constitutive response of precipitated NiTiHf SMAs, in this work a finite element based micromechanical modeling framework is developed. Two types of representative volume elements are considered: (i) exact 3-D reconstructions of precipitates using transmission electron microscopy, and (ii) less expensive ellipsoidal representation of precipitates. The composition changes in the material are modeled, and their effects are incorporated by considering composition dependency of phase transformation properties in the matrix. The resulting model is used to predict the constitutive responses for different aging conditions in Ni_{50.3}Ti_{29.7}Hf₂₀ and Ni_{50.3}Ti_{34.7}Hf₁₅ SMAs. The model predictions are in good agreement with the experimental measurements, and experimental and modeling results are presented with confidence intervals from sample-to-sample variations. The present work constitutes the first micromechanical modeling of high temperature SMAs with consideration of real microstructures.

© 2022 Acta Materialia Inc. Published by Elsevier Ltd. All rights reserved.

1. Introduction

Shape Memory Alloys (SMAs) are active materials which can undergo a diffussionless, thermo-elastic solid-to-solid martensitic phase transformation. This happens between low temperature martensitic phase and high temperature austenitic phase, and is induced by variations in temperature, stress or both [1]. Due to their ability to recover from high strains and transform against high stress, they are suitable for designing solid-state actuators of high work density [2,3]. SMAs are used in many engineering applications: as actuators, morphing structures in aerospace engineering [4–8], passive energy dissipators and vibration dissipators in civil engineering [9–11], and for designing stents, micro-devices and implantable devices in biomedical engineering [12–16].

Depending on the application, SMAs are chosen for transformation properties fitting the operating temperature range. Among

Corresponding author.

E-mail address: lagoudas@tamu.edu (D.C. Lagoudas).

the various SMA materials known, the NiTi SMAs are commonly used because of their high strength, high transformation strain and lower permanent deformation during actuation. Despite possessing these desirable transformation characteristics, the NiTi SMAs cannot martensitically transform above 100 °C. On the other hand, Ni-TiHf High Temperature Shape Memory Alloys (HTSMAs) can transform at temperatures higher than 100 °C [17]. Depending on the composition of the alloying elements, they can exhibit shape memory behavior in a wide range of temperatures (\sim -50 °C to 500 °C) [18–23]. The lower material cost compared to other HTSMAs with precious metals, and ability to exhibit high actuation energy density, make NiTiHf SMAs a good choice to design robust and efficient high temperature solid-state actuator systems [17,24–27].

Recent discoveries show that aging heat treatments in NiTiHf SMAs lead to the formation of nano-sized precipitates termed as h-phase [28]. The presence of precipitates modify the actuation behavior of the SMA with different phase transformation properties (transformation temperatures and magnitude of recoverable strain) [29–31]. On one hand, as the precipitates are coherently formed

and do not phase transform [32], they restrain the maximum possible phase transformation in the matrix. On the other hand, as the precipitation happens through elemental diffusion, the composition of the matrix phase changes during the precipitation. Since the NiTiHf SMAs are sensitive to the composition, these compositional variations affect the phase transformation properties of the matrix and consequently the effective response.

The aging heat treatments can create the samples with desired precipitation topology and modify the transformation behavior in NiTiHf SMAs. As the NiTiHf SMA material system exhibit phase transformation in a wide temperature range with changing composition, the precipitation in NiTiHf produces SMAs that can phase transform in a range of temperatures because of the compositional variations in the matrix. Hence, the aging heat treatments in Ni-TiHf can be a powerful method to design and fine-tune SMA actuators for a specific application. The precipitation in NiTiHf can also stabilize its cyclic actuation response by reducing transformation induced plasticity during multiple thermal cycling [33], which makes the heat treatment modifications desirable. Presently, the constitutive response of NiTiHf SMA is known only for limited compositions and aging paths due to the time and cost associated with the testing. The SMA designing process can be accelerated with the help of virtual computational models that can predict the dependency of the transformation characteristics on the heat treatment beforehand.

Micromechanical modeling has been successfully used in the past to predict the SMA responses. The geometry and mechanical properties of the phases, the interaction between the phases, and bridging these small-scale individual phenomena to the imposed macroscopic loading conditions are key aspects in developing such micromechanical models. Many of the past works used orientation averaging techniques or mean field approaches such as the Mori-Tanaka approximation to model the SMA response in the presence of precipitates [34–40]. These methods were limited to capturing the effects of regular precipitate shapes and simple interactions. In recent years, Finite Element Analysis (FEA) based full-field modeling using the approach of Representative Volume Elements (RVEs) is found to be effective not only in capturing the effects of irregular shapes of precipitates but also capable of predicting the effects due to compositional variations in the NiTi SMA systems [41–45].

In the current work, an FEA based full-field micromechanical model is developed to predict the precipitation hardened NiTiHf SMA actuation response from the precipitate microstructure. RVEs of the SMA microstructure were generated in the following two ways: (1) 3-D reconstructions of the precipitates from TEM micrographs and (2) approximated ellipsoidal precipitates RVEs. Constructing RVEs from the TEM sample is an expensive process, but it gives the real 3-D microstructure, while constructing RVEs using ellipsoids is an approximated description but is less expensive. Using the approximated ellipsoidal method helps in studying the effects due to microstructural variations, as they are easy to generate. In both RVEs, the precipitates were modeled as nontransforming elastic material and surrounded by polycrystalline phase-transforming matrix. The matrix was modeled using the Lagoudas et al. [46] constitutive model, and the precipitates using isotropic elastic behavior. In the thermo-mechanical constitutive model of the matrix, the compositional effects were incorporated by considering the composition dependency of the phase transformation properties. The effects of residual stress arising from lattice mismatch and the difference in elastic properties between the phases were also accounted for.

The resulting FEA micromechanical model was then used to analyze the actuation behavior in aged NiTiHf samples for different heat treatments from the physics and modeling perspectives. The precipitation hardened responses of Ni_{50.3}Ti_{29.7}Hf₂₀ SMA were modeled, and the behavior was analyzed in terms of the mi-

crostructure and composition changes. Estimation of composition effects, stiffness of the precipitate phase and material parameters of the matrix phase were carried out through calibration using the FEA model. The 3-D reconstructions studied in this work focus on shorter heat treatments and varying volume fractions compared to previous efforts [28,47], where the focus was on very long heat treatments. This work presents the first modeling study on the actuation response of HTSMAs considering realistic 3-D microstructures. Knowledge of the real microstructures from the 3-D reconstructions helped to validate the methodology for ellipsoidal shaped RVEs. Experiments conducted on multiple samples of solutionized (unprecipitated) and heat treated Ni_{50 3}Ti_{29 7}Hf₂₀ SMA were used to analyze the sample-to-sample variation. In addition, the ellipsoidal RVE methodology was used for modeling the heat treatment responses in two other SMAs available in the literature [48] with compositions $Ni_{50.3}Ti_{29.7}Hf_{20}$ and $Ni_{50.3}Ti_{34.7}Hf_{15}$, but with a different processing history. The comparison of simulations and experiments demonstrates that the proposed micromechanical model framework accurately predicts the precipitation hardened response and will be extremely useful in designing aging heat treatments in NiTiHf SMAs.

The paper is structured as follows. Section 2 describes the microstructural observations from TEM study in NiTiHf in different heat treated samples. 3-D reconstructions of the microstructure, volume fraction estimation and the precipitate morphology are shown. Section 3 describes the experimental observation of actuation responses in precipitation-hardened NiTiHf and discusses the mechanisms through which the precipitates can modify the actuation response. Section 4 discusses the key steps in the developed micromechanical model. Section 5 discusses the steps involved in building approximate RVEs with ellipsoidal precipitate shapes. Section 6 explains the calibration of model parameters from the experimental responses. Section 7 discusses the comparison of experiments and predictions. Section 8 summarizes the main conclusions from the work.

2. Microstructure in NiTiHf and 3-D reconstruction

An accurate description of the precipitate microstructure and measurements of the volume fraction of precipitates is needed in the micromechanical modeling. Regular TEM and scanning TEM (STEM) micrographs display only the 2-D projection of 3-D objects, and cannot give a complete picture of the shape of precipitates. The volume fraction of the precipitates, which is critical information required in the modeling, cannot be estimated accurately from the 2-D representations. To overcome these difficulties, 3-D reconstructions of the microstructures were generated. In this section, the procedure used for these reconstructions, the key observations and estimation of volume fraction are discussed.

2.1. Experimental procedure

Elemental Ni, Ti, and Hf (99.98%, 99.95% and 99.9% in purity, respectively) were used to fabricate a Ni-rich Ni $_{50.3}$ Ti $_{29.7}$ Hf $_{20}$ (at.%) SMA via vacuum induction melting. The material was then vacuum homogenized at 1050 °C for 72 hours and air cooled. The ingot was hot forged to an R ratio of 2.35:1 followed by cooling in the air. The samples cut using wire electrical discharge machining (EDM) were then solution heat treated (SHT) at 900 °C for 1 h followed by water quenching. The samples were then heat treated at 550 °C, 600 °C and 650 °C for 10 hours followed by air cooling to grow precipitates with various sizes and volume fractions. The TEM specimens from the bulk samples were mechanically polished using 1200-grid silicon carbide papers and punched into 3 mm TEM discs with a thickness around 100 μ m. These discs were then twin-jet electropolished using a Tenupol-5 polishing system with a

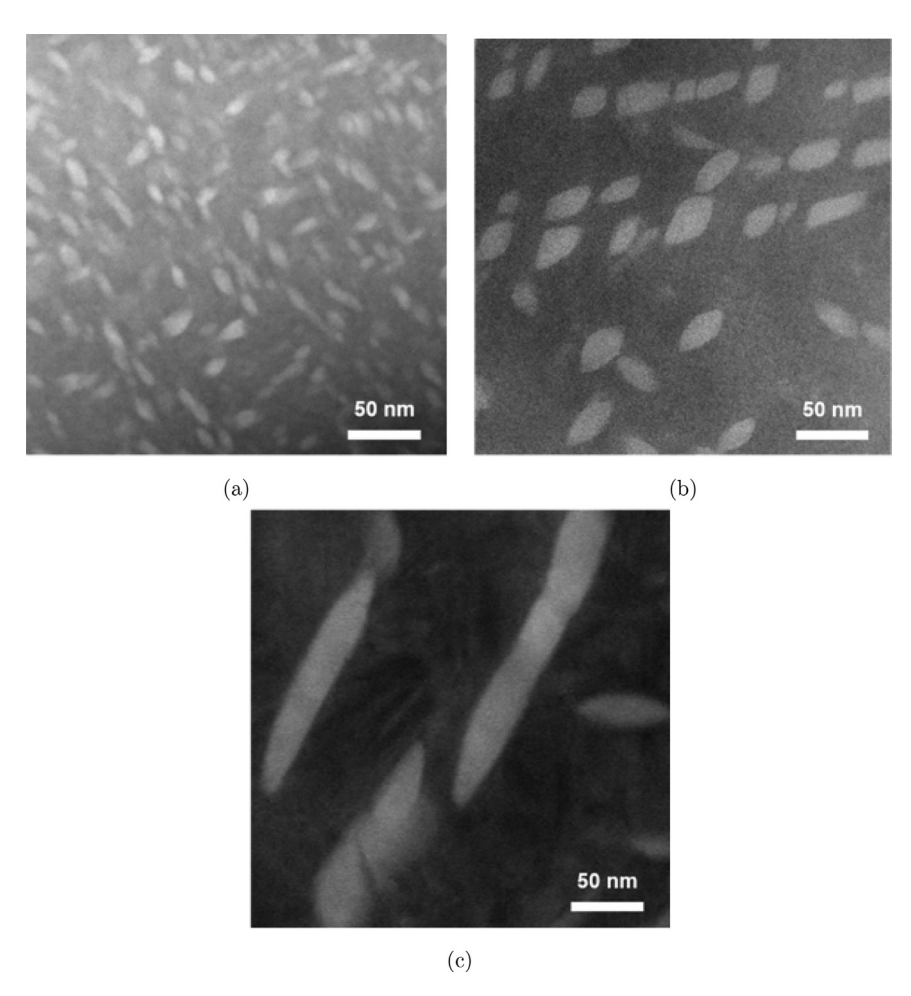


Fig. 1. HAADF-STEM images of $Ni_{50.3}Ti_{29.7}Hf_{20}$ heat treated at (a) $550\,^{\circ}\text{C}$ for 10h, (b) $600\,^{\circ}\text{C}$ for 10h and (c) $650\,^{\circ}\text{C}$ for 10h.

solution of 30% nitric acid in ethanol at -30° C. High-angle annular dark-field scanning transmission electron microscopy (HAADF-STEM) micrographs were acquired near the perforation to characterize the precipitates using a FEI Tecnai G2 F20 Super-Twin FE TEM operating at 200 keV. 3-D models of precipitates were reconstructed from the HAADF-STEM images using TEM tomography. The micrographs were taken under different magnifications to ensure similar amounts of precipitates were captured in the view field. The tomographic tilt series were collected over 90° at 2° intervals. Image alignment and 3-D reconstruction were performed using open-source tomography platform Tomviz with a 'weighted back projection' algorithm [49]. The detailed process is described in Levin et al. [50]. The reconstructed 3-D models were then imported into the Paraview software [51], where the visualization and analysis were performed.

2.2. Microstructure in 2-D HAADF-STEM

Precipitates of different sizes and number densities were observed in the heat-treated SMAs. The HAADF micrographs shown in Fig. 1 were taken at the same magnification for direct comparison. In all samples, the precipitates appear to be brighter. Such contrast mainly comes from the higher Hf content in the precipitates than in the matrix. Fig. 1(a) illuminates a high density of nano-precipitates with \sim 10 nm in size in the 550 °C heat-treated NiTiHf. Increasing the heat treatment temperature to 600 °C, the precipitates grow to \sim 30 nm in size with a decreasing number density (Fig. 1(b)). Further, increasing the heat treatment temperature to 650 °C results in even larger precipitates (\sim 150 nm

long) and lower number density (Fig. 1(c)). In contrast to the non-uniform precipitate distribution in NiTi [52] with differences at the grain interior and grain boundary, the precipitate distribution in NiTiHf were observed to be more uniform. The difference between NiTi and NiTiHf can be explained by their differences in precipitation kinetics. In NiTi, the precipitates form directly from the solute via heterogeneous nucleation on crystallographic defects, whereas in NiTiHf, the solute atoms form Guinier-Preston (GP) zones first and the GP zones then evolve into precipitates, which creates a more uniform distribution of precipitates.

TEM studies on the precipitates showed coherency between the precipitate and the austenite B2 matrix, with continuity of the atomic planes across the precipitate interfaces over large distances more than 50 nm [29,53]. The heat treatments 550°C 10h and 600°C 10h produce precipitates smaller than 50 nm, which can be assumed coherent with the matrix. Whereas, the heat treatment 650°C 10h produce precipitates of 200 nm size that may lose some coherency. However, the extent of incoherency is difficult to be measured. Preliminary calculations performed by the authors indicates that a loss of coherency causing up to 20% loss of precipitate stiffness do not modify the responses significantly. Thus, in the modeling, a complete coherency was assumed owing to the better coherency properties in the h-phase precipitates.

2.3. Microstructure in 3-D reconstructions

TEM-based tomography was used to extract the 3-D microstructural features of the precipitates. Fig. 2 show the 3-D reconstruction of the microstructures in the 3 heat treatments studied (for

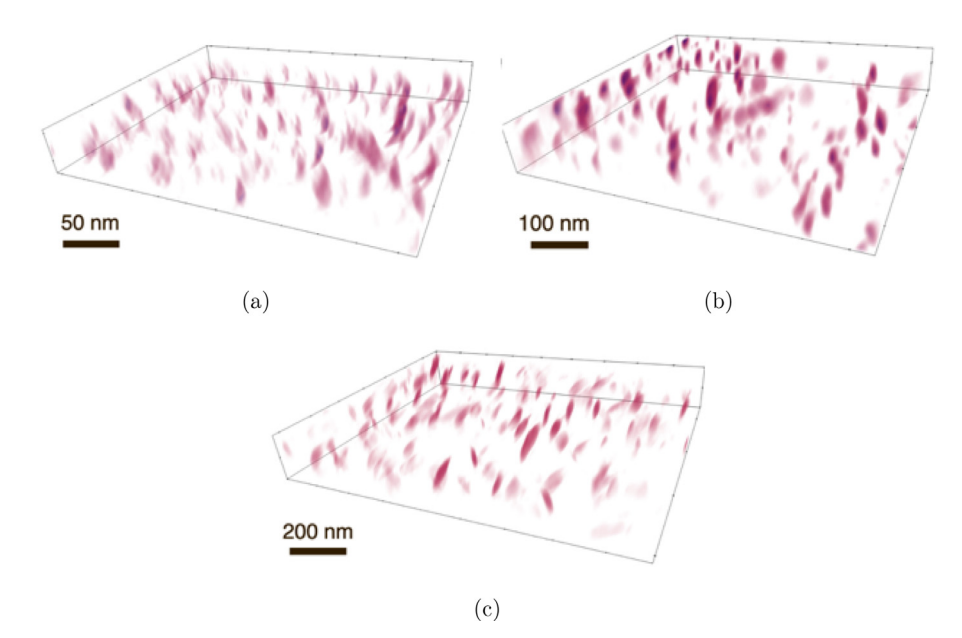


Fig. 2. 3-D reconstructions from HAADF-STEM images of precipitation hardened Ni_{50.3}Ti_{29.7}Hf₂₀ showing microstructures in different heat treatments: (a) 550 °C for 10h, (b) 600 °C for 10h, and 650 °C for 10h.

videos, refer to supplementary information). The precipitate volume fractions were calculated from the 3-D reconstruction as the ratio of grids in the precipitate region to the total grids. The volume fractions were estimated to be $8.5\pm0.3\%$, $9.8\pm3\%$ and $12.9\pm2.5\%$ for the heat treatments at $550\,^{\circ}\text{C}$, $600\,^{\circ}\text{C}$, and $650\,^{\circ}\text{C}$ respectively. The error bars reported were the spatial variation from four divisions of the whole volumes in the reconstruction. The increase in precipitate volume fraction from $550\,^{\circ}\text{C}$ to $650\,^{\circ}\text{C}$ indicates excess amount of solute atoms (Hf and Ni) in the matrix and the precipitation has not saturated. Morphology of individual precipitates was extracted from the 3-D reconstructions using cluster analysis in MATLAB software [54]. The selected precipitate shapes from each heat treatment are shown in Fig. 3. The precipitate shapes were observed to be close to that of platelet or curved prolate ellipsoidal geometry.

Compared to other methods like Focused Ion Beam (FIB) Scanning Electron Microscopy (SEM) 3-D slice-and-view [52], the TEMbased tomography has advantages and disadvantages. FIB is not suitable for the current heat treatment cases in the NiTiHf SMA, especially in the lower aging temperature cases (e.g., 550 °C) as the precipitates are too small (few nm in width and ~20 nm in length) to be resolved in the SEM. Moreover, the smallest slicing thickness in FIB is 5 nm and many precipitates will only constitute one voxel, which is difficult to distinguish from the noise. When compared to the FIB-based 3-D slice and view approach, the TEM-based tomography method may contain "missing wedges" due to the physical limitation of how much the TEM holder can tilt, although this should not significantly affect the measurement accuracy. To assess the accuracy of the volume fraction estimates in the TEM-based tomography requires a standard sample with known precipitate volume fraction, which was not available. Nonetheless, the accuracy of the TEM-based volume fraction estimate can be assumed to be satisfactory, as it is a well-established technique based on the Radon transformation.

3. Actuation response in precipitation hardened NiTiHf SMAs

The presence of precipitates in NiTiHf SMAs has been shown to change actuation behavior by modifying transformation temperatures, recoverable strain and reducing transformation induced plas-

ticity [24,31,55,56]. Yang et al. [28] measured the precipitate composition as Ni_{53.62}Ti_{20.03}Hf_{26.35} using atom probe tomography in Ni_{50.3}Ti_{29.7}Hf₂₀ heat treated at 600 °C for 815 hours. Since the precipitate phase has higher concentration of Ni and Hf, it results in a Ni-lean and Hf-lean matrix in the aged SMA compared to the solutionized as a result of atomic diffusion during precipitation. The hphase precipitates maintain coherency with the matrix [29,53]. All these aspects of the aged NiTiHf SMA can affect the phase transformation behavior.

An actuation loading path for the SMAs in a temperature-stress phase diagram and a typical strain - temperature response are shown in Fig. 4. The loading path indicated (blue dashed line from A to B and B to A) in Fig. 4(a) represents the cooling and heating of the material in the presence of a fixed load. The material then transforms between the high temperature austenitic phase (A) and the low temperature martensitic phase (B). An example of the resulting actuation response is shown in Fig. 4(b). The phase transformations produce a sudden expansion or contraction in the strain response, which is captured using the transformation strain parameter ($H^{cur}(\sigma)$) in the Lagoudas et al. [46] constitutive model. The temperature ranges of transformation are described with transformation temperature (TT) parameters. The four TTs are calculated from the response using tangent lines approach [1] shown in Fig. 4(b).

The actuation responses in heat treated $Ni_{50.3}Ti_{29.7}Hf_{20}$ SMAs were measured with the following experimental procedure. Dogbone shaped tension samples with 1.5 mm x 3 mm x 8 mm gauge sections were cut from the $Ni_{50.3}Ti_{29.7}Hf_{20}$ ingot using wire EDM and used for load-biased thermal cycling (actuation) experiments. The samples were subjected to solution heat treatment (SHT) at $900\,^{\circ}\text{C}$ for 1h in argon and water quenched (WQ) to dissolve any possible secondary phases formed during fabrication. Further, the aging heat treatments were performed to create precipitation. Actuation experiments were performed on the solutionized and precipitation hardened samples to compare the change with precipitation.

In actuation experiments, the tension samples were loaded to different stress levels in the fully austenitic state and thermally cycled between ambient temperature and a temperature significantly above the austenite finish temperature. Two to three repetitions

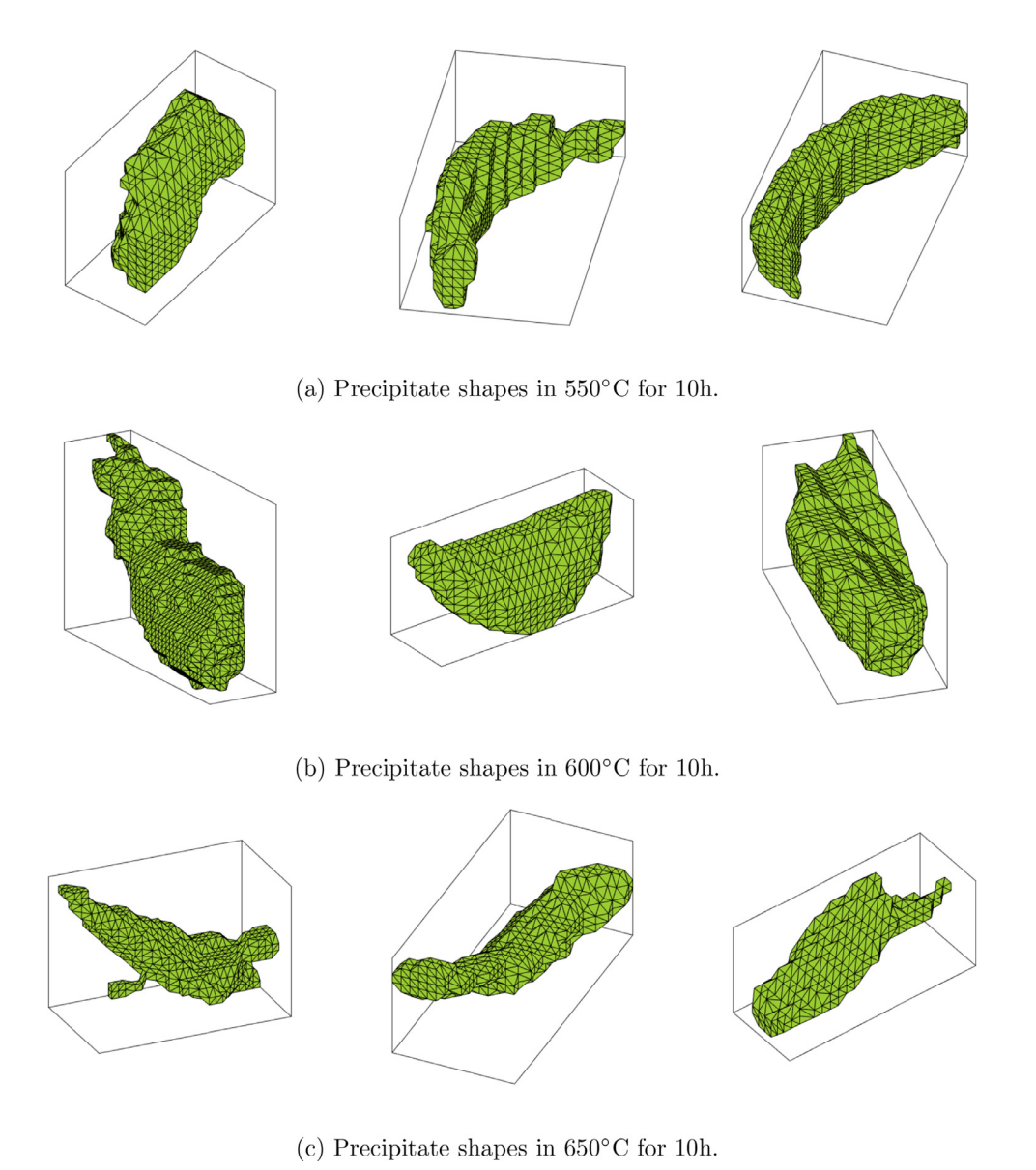


Fig. 3. Individual precipitate morphology extracted from the 3-D reconstructions of precipitation hardened Ni_{50.3}Ti_{29.7}Hf₂₀ SMAs.

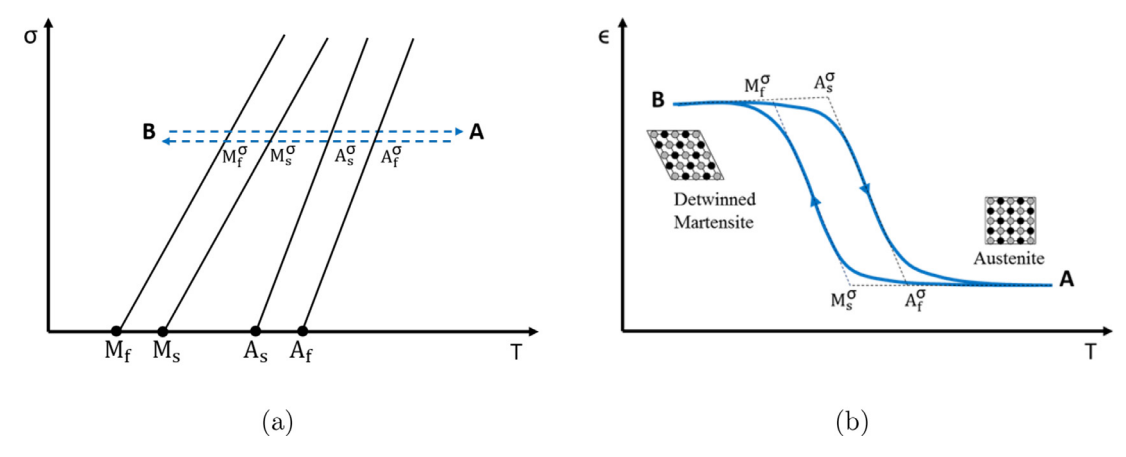


Fig. 4. Actuation loading path and response: a) loading path shown on a typical temperature-stress phase diagram, and b) a representative strain - temperature response shown with the tangent line approach to determine the phase transformation temperatures.

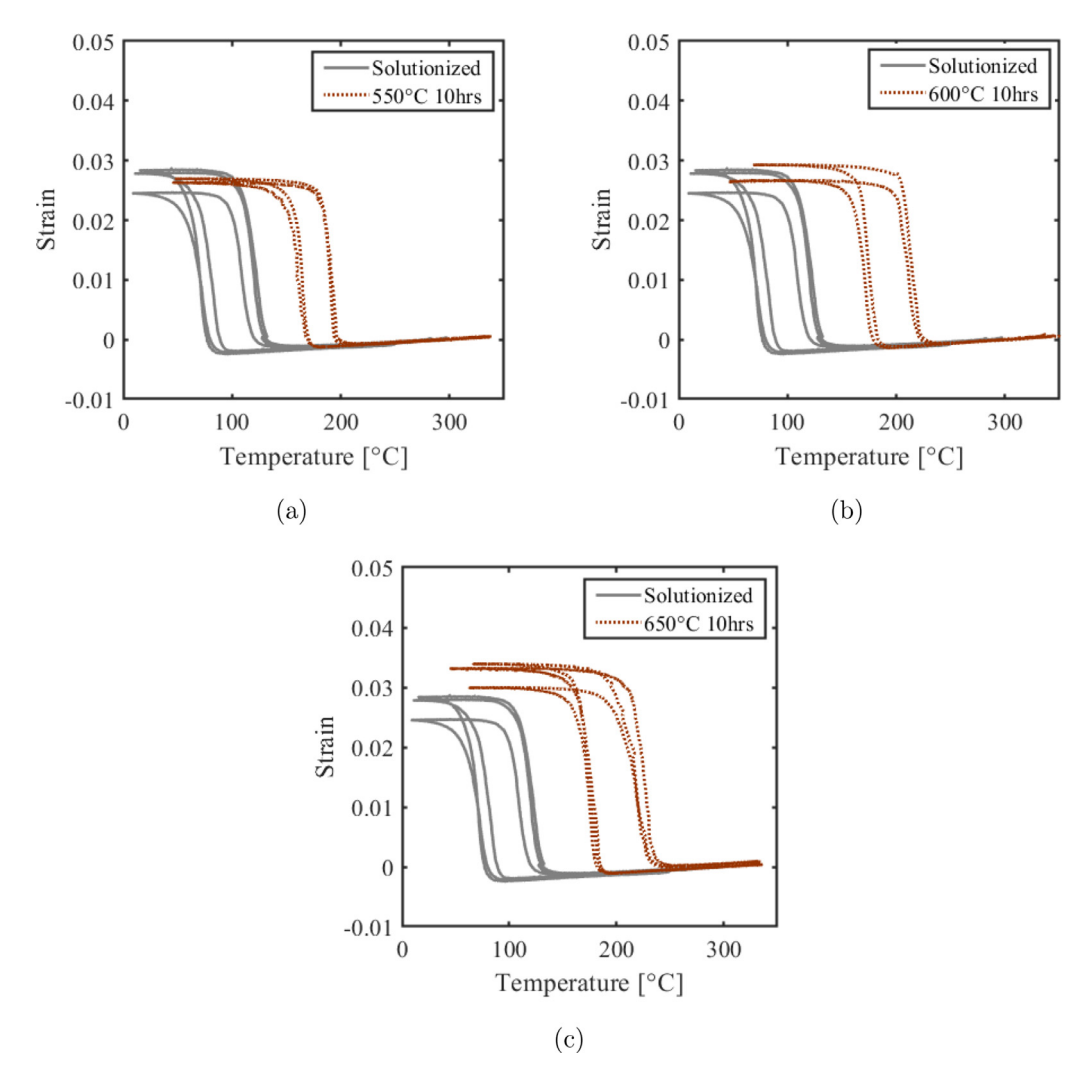


Fig. 5. Comparison of thermomechanical behavior of Ni_{50.3}Ti_{29.7}Hf₂₀ heat treated at (a) 550 °C, (b) 600 °C and (c) 650 °C for 10 hours at 200 MPa. The response from multiple samples demonstrates the sample-to-sample variation in the material behavior.

were performed using different samples to check the sample-to-sample variation. The experiments were carried out using a servo-hydraulic MTS test frame, where the specimens were conductively cooled by flowing liquid nitrogen through copper tubing wrapped around the grips and heated via resistive heating bands. The heating and cooling rates were 8–10 °C min⁻¹ and the sample temperature was measured using a K-type thermocouple attached directly to the samples gauge section. The change in axial strain during the thermal cycles was recorded with an MTS high-temperature extensometer attached directly to the gauge section of the specimen.

Fig. 5 shows the comparisons of tensile actuation responses in Ni $_{50.3}$ Ti $_{29.7}$ Hf $_{20}$ heat treated at 550 °C, 600 °C and 650 °C for 10 hours. The comparisons show the phase transformation in the heat treated materials are happening at much higher temperatures than the solutionized material. Also, the maximum strain in these responses is increasing with the heat treatment from 550 °C to 650 °C (Fig. 5(a)-(c)). A higher strain is observed in the aged material response compared to the solutionized responses in the 600 °C and 650 °C cases. This trend is counterintuitive, as it is generally expected that the non transforming precipitates [32] in these precipitation hardened materials impede phase transformation. Similar increase in strain was reported in the work of Evirgen [48] on two NiTiHf compositions (Ni $_{50.3}$ Ti $_{29.7}$ Hf $_{20}$ and Ni $_{50.3}$ Ti $_{34.7}$ Hf $_{15}$) as well, which are discussed in the upcoming sections and in the results (Section 7).

Higher transformation temperatures in the aged NiTi and Ni-TiHf have been well studied in the literature and are attributed to compositional changes in the matrix of the precipitation hardened material [18,42,57,58]. While the increase in transformation strain in aged SMA has not been well studied, some similar trends of increasing transformation strain have been observed in NiTi. In the work of Kim and Miyazaki [59] on Ti-50.9at,%Ni SMAs, it was seen that transformation strain increased from non-precipitated to precipitated alloy (aging at 100 °C to 200 °C).

In the work of Hamilton et al. [60], it was seen that Ti-50.4 at.%Ni [0 0 1] single crystals produced higher strain in 550°C 1.5h aging compared to its solutionized response. This behavior is similar to what is seen in the NiTiHf, where increasing heat treatment gives higher transformation strain. To model the aged material response coherently with all these observed phenomenons, the following microstructural mechanisms were identified.

• The Ni-lean and Hf-lean matrix in the NiTiHf create higher transformation temperatures (TTs) in the matrix, which is reflected in phase transformation occurring at higher temperatures in the aged SMA (see Fig. 5). In NiTiHf SMAs, the TTs are highly sensitive to composition and changes in the order of few percentages can shift the behavior in the order of 100 °C [18,61].

As the precipitates are coherent with the matrix [29,53], they
create residual stress in the matrix. Since the phase transformation is sensitive to stress, the residual stress can increase the
TTs [62].

- The coherent non-transforming precipitates restrain the transformation in the surrounding matrix. Consequently, a higher driving force is required for complete transformation, which is reflected as a decrease in the forward transformation temperatures [63].
- In addition to the composition dependency of TTs, a dependency of transformation strain on composition is hypothesized. The Ni-lean and Hf-lean matrix creates higher transformation strain in the matrix. As a result, the competition of constraining effects of the precipitate and the increasing transformation strain in the matrix determines the increase or decrease of maximum strain in the aged SMA response compared to the solutionized response. More on the composition dependency of transformation strain and calibration is discussed in Section 6.2.2.

These identified mechanisms are incorporated into the micromechanical model and are discussed further in the next section.

4. Micromechanical modeling using 3-D reconstructions

A finite element based micromechanical model was developed to model the actuation response in precipitation hardened NiTiHf SMAs. RVEs of the material microstructure extracted from the 3-D reconstructions were modeled with different constitutive behaviors in the precipitate and the matrix regions. The matrix was modeled as polycrystal phase transforming material and the precipitates as linear elastic material. The residual stress due to coherency and the composition change in the matrix due to diffusion were computed and used as inputs in the model. Finally, the actuation response was computed by applying boundary conditions on the RVE.

In the current modeling, a phenomenological approach for predicting the precipitation hardened polycrystal SMA response is used. In the actual material microstructure, the precipitates are present in single crystal grains within a polycrystal containing many grains, whereas in the current framework, the grain or grain level interactions are not modeled, but modeled as precipitates in an effective polycrystal matrix. Compared to a multiscale homogenization approach, the authors assume that accuracy is not compromised in the phenomenological approach towards predicting the effective precipitation hardened polycrystal SMA response. The authors compared the effective stiffness value for a precipitation-hardened polycrystal solved with two approaches: 1) as a multiscale homogenization problem with 200 grains and 2) as a phenomenological homogenization approach with precipitates in the effective polycrystal matrix. The properties were chosen such that they reflect the tangent stiffness in phase transformation. The two methods gave close predictions of effective stiffness (see Appendix A) in agreement with the assumption in the phenomenological approach.

The main steps in the developed micromechanical model are: 1) generating RVEs, 2) modeling the matrix phase and precipitate phase, 3) Characterizing matrix composition, 4) solving for internal stresses, and 5) solving the RVE boundary value problem to predict the actuation. Fig. 6 shows a summary of the simulation process, where the RVEs are created using the TEM 3-D reconstructions, and the actuation behavior is solved using FEA. The SMA actuator responses were predicted in the ABAQUS software [64] with the application of thermomechanical boundary conditions. Steps in the micromechanical model are discussed in the following subsections.

4.1. RVE generation

The RVEs were created from the TEM microstructure representations explained in Section 2. Fig. 6 shows a RVE extracted from the complete microstructure in the 550 °C for 10h heat treatment case. The pixel representation of the 3-D reconstructions were imported as structured voxel mesh. The precipitate regions were identified and assigned the precipitate properties, and the remaining region was assigned to be the phase transforming matrix. From each 3-D reconstruction of the heat treatment case, four smaller RVEs were created. The multiple realization simulated how the microstructural variation affects the effective response.

4.2. Matrix and precipitate material models

The phase transforming matrix was modeled using the polycrystalline constitutive model of Lagoudas et al. [46]. The constitutive model was implemented using the User Material (UMAT) subroutine feature in ABAQUS software [64]. The precipitates were modeled as linear elastic with isotropic stiffness properties, and implemented using the default material model in ABAQUS. The phase transformation properties of the matrix and precipitate stiffness were obtained through calibration. More on the calibration is explained in Section 6.

4.3. Composition of the phase transforming matrix

The composition profiles in the matrix are the result of the Fickian diffusion during precipitation. These profiles will not change significantly during thermal cycling, as the kinetics of diffusion is very low at the thermal cycling temperatures. In the current modeling, the composition profiles were approximated by the average composition of the matrix, though in the actual material there are gradients around the precipitates. The average composition of the matrix (C_m) was calculated in terms of the volume fraction of precipitates (VF) and the solutionized material composition (C_0) using the following atomic balance equation.

$$C_m = \frac{C_0 - VF * C_p}{1 - VF},\tag{1}$$

where, C_P is the composition of the precipitate which can be taken as Ni_{53.62}Ti_{20.03}Hf_{26.35} based on the measurements of Yang et al. [28]. Equation (1) represents a set of three equations on Ni, Ti and Hf contents as the atomic balance is separately satisfied in each element for the same volume fraction. In each TEM based RVE modeled, the average matrix composition was calculated from the corresponding measured volume fraction in the RVE.

4.4. Residual stress calculations

The internal stresses in the material are created from two sources: the lattice misfit between the phases and the misfit in the elastic stiffness between the phases. The internal stress from the lattice misfit is resulted during precipitation and remains constant during loading, so are termed as residual stress. The internal stress due to elastic stiffness evolves during the loading and phase transformation, and are accounted inherent in the finite element model. The residual stress distribution due to the lattice misfit between the precipitate and the matrix phases was solved by applying an equivalent eigenstrain on the precipitates. This was solved as a problem using the idea that a difference in thermal expansion coefficients in the matrix and precipitate can simulate eigenstrain in a pure thermal loading. A difference in the thermal expansion coefficients corresponding to the eigenstrain value was applied to the two phases, and a corresponding pure thermal heating step was used to solve the residual stress distributions. This was done

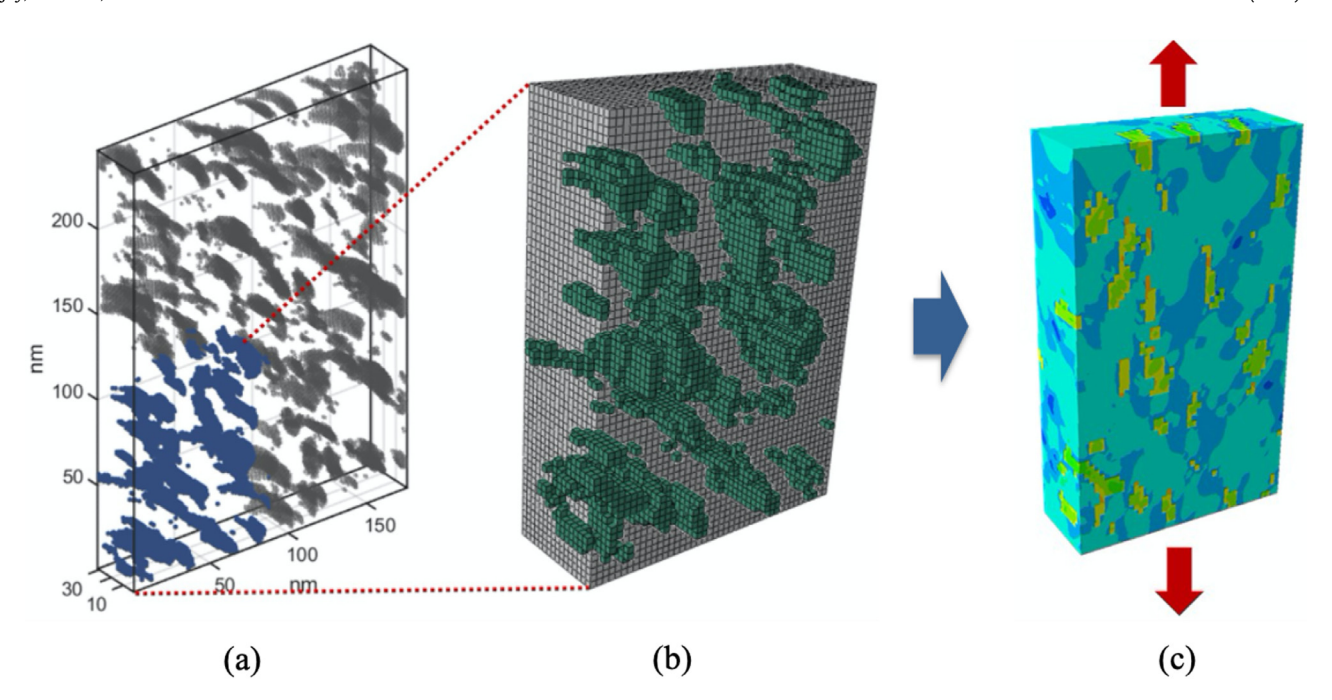


Fig. 6. Micromechanical modeling showing the RVE creation from the 3-D reconstruction and FEA simulation to solve the effective response. (a) The full 3-D reconstruction, (b) one of the four RVEs taken from the reconstruction and (c) FEA simulation of the RVE along an in-plane loading direction.

using FEA in ABAQUS software, and the solution of residual stress distribution was introduced as an initial condition in the overall solution process. For the current work, the eigenstrain in the precipitates was calculated to be 0.01 hydrostatic strain based on the 1% lattice misfit between the two phases [53]. Here, only the hydrostatic components were considered, assuming a similarity with NiTi eigenstrain [65].

4.5. Solving the thermo-mechanical response from the RVEs

The actuation responses of the aged NiTiHf SMAs were simulated by applying temperature and stress boundary conditions on the RVEs according to the actuation loading path (Fig. 4(a)). A constant stress corresponding to the actuation was applied on the RVE in the loading direction. The heating-cooling thermal environments were simulated by changing the temperature boundary condition for the entire volume. In addition, the periodic boundary conditions were applied on the faces of the RVEs to avoid the boundary effect and to predict pure bulk constitutive behavior. The RVE deformation was solved through FEA using implicit formulation in the ABAQUS FEA software [64]. The effective response was calculated from the volume average in the RVE. The responses were calculated along two in-plane loading directions in the TEM microstructure to capture the variability. The through-the-thickness loading was not included, as there might be thickness effect due to the comparable size of precipitate to thickness. Actuation responses for three different stress levels (100 MPa, 200 MPa and 300 MPa) were simulated.

5. Modeling with ellipsoidal RVEs

As the TEM reconstructions (Section 2) show that the precipitate shapes are closer to curved prolate ellipsoid, a less expensive modeling methodology with RVEs of ellipsoidal shape is proposed. As an alternative to volume fraction estimation from the 3-D reconstruction, here the volume fraction is estimated from shifts in differential scanning calorimetry (DSC) measurements of the precipitated SMA using composition-transformation temperatures (C-TT) relations. The ellipsoidal precipitate shapes are approximated

from the 2-D TEM instead of using the 3-D reconstructions. These steps are discussed in the following subsections.

5.1. Estimation of matrix composition and volume fraction from calorimetric measurements

The matrix composition in the aged material was estimated comparing its DSC based TTs with C-TT relations, and the volume fraction was computed from the matrix composition utilizing atomic balance (Eq. 1). First, the transformation temperatures of the aged SMA in the stress-free state were calculated from peaks in forward and reverse transformations from their DSC responses [18]. Because DSC measurements are performed in a stress-free material, the effects of stress concentration can be expected to be minimal, and the transformation peaks are mostly dictated by the matrix transformation. With this assumption, the TTs of the precipitation-hardened SMAs can be correlated to its matrix phase composition, as only the matrix is phase transforming. Hence, using the C-TT relations, the average matrix composition is determined to be the one which give TTs closer to those measured. Fig. 7(a) shows an example of estimating average composition in the modeling of precipitation-hardened NiTi SMAs [42], where, C_0 is the composition before precipitation and C_M is the average composition in the matrix after precipitation.

For NiTiHf SMAs, the C-TT relations based on the extensive DSC measurements conducted by Umale et al. [18] were used. The 2-D Thin-Plate Smoothing Splines in MATLAB software [54] were used for fitting and interpolation. Fig. 8 shows the variation of M_s with composition in NiTiHf SMAs in the work of Umale et al. [18]. For a given M_s measured, one can identify many Ni and Hf values that would result in the same value (see Fig. 8) as opposed to a single Ni composition in the case of binary NiTi SMAs. Therefore, we used all four transformation temperatures to find the best composition that would fit the DSC measured TTs. For this, a constraint optimization on the C-TT relations (summarized in Eq. 2) was used, where the constraint ensured atomic balance for Ni and Hf. The mean squared error (MSE) between the measured TTs in the aged material $(M_s^{ag}, M_f^{ag}, A_s^{ag}$ and A_f^{ag}) and the values from the C-TT re-

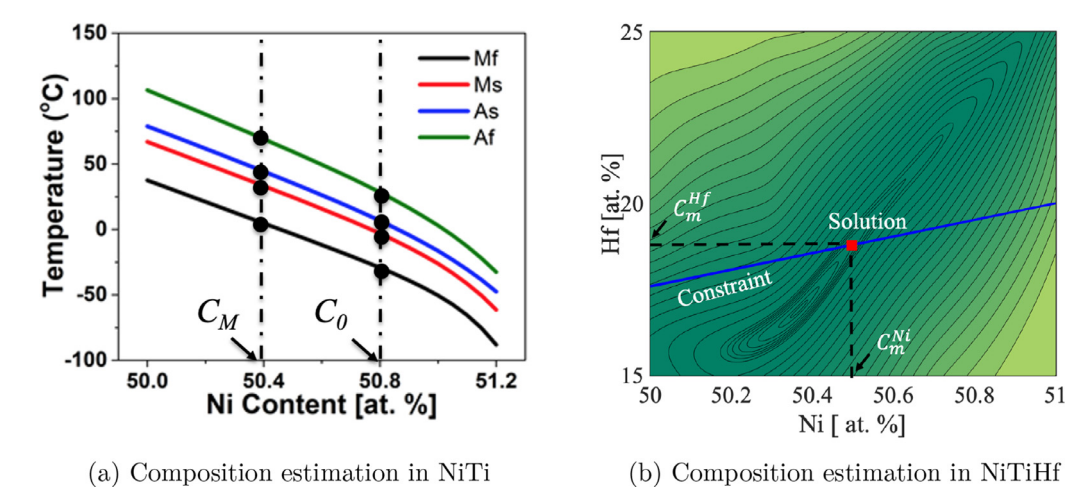


Fig. 7. Figure showing the estimation of the average matrix composition from TTs using C-TT relations in (a) NiTi SMA [44,66] and (b) NiTiHf SMA. In NiTiHf, a constrained optimization on mean squared error (MSE) gave better estimations.

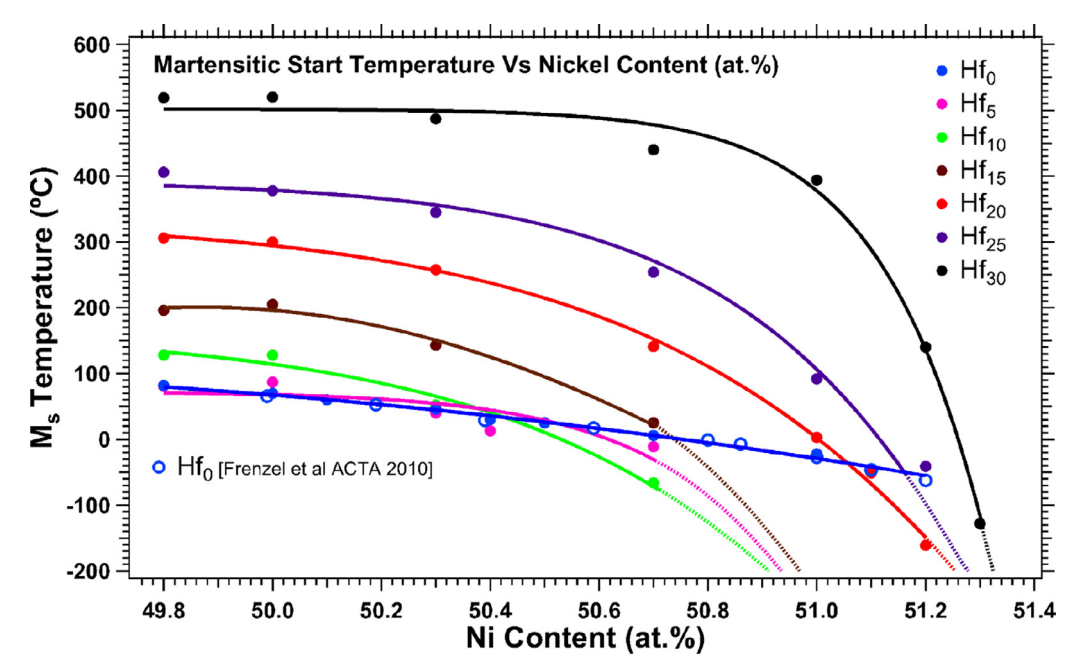


Fig. 8. Variation of martensitic start temperature (M_s) with Ni and Hf composition in NiTiHf SMAs. Reprinted from Umale et al. [18], Copyright 2019, with permission from Elsevier.

lations are minimized to find the optimum value of composition. The whole process is summarized as:

$$\begin{bmatrix} C_m^{Ni}, C_m^{Hf} \end{bmatrix} = \min_{C^{Ni}, C^{Hf}} \left(\frac{1}{4} \sum_{TT = M_s, M_f, A_s, A_f} \left(TT^{ag} - TT^{CTT} (C^{Ni}, C^{Hf}) \right)^2 \right) \\
\text{s.t.} \left(\frac{C_0^{Ni} - C^{Ni}}{C_p^{Ni} - C^{Ni}} \right) = \left(\frac{C_0^{Hf} - C^{Hf}}{C_p^{Hf} - C^{Hf}} \right)$$
(2)

where, C_m is the matrix composition, C_0 is the solutionized material composition, C_P is the precipitate composition, and the 'TT' refer to the four TTs. The superscripts 'Ni' and 'Hf' refer to the specific components, and the superscripts 'ag' and 'CTT' refer to the values measured for the aged SMA and values from the C-TT relations, respectively. The constraint equation makes sure the atomic balance is satisfied in both Ni and Hf for the same volume fraction. An example of the minimization problem for 600 °C 10h is summarized in the MSE contour plot shown in Fig. 7(b), where the solution is the optimum from the constrained minimization. The

optimization problem (Eq. 2) was solved for all heat treatments. The results are summarized in Table 1 and compared with values measured in the 3-D reconstructions (Section 2.3). For the two lower heat treatments, the volume fraction estimation is close to the measured value, but considerably different in the 650 °C 10h heat treatment. One of the reasons for this discrepancy is that the precipitate composition is assumed to be constant in the current estimation, despite the fact that it is known to be a function of the initial composition and heating conditions [53]. For example, the calculation with a precipitate composition Ni_{52.9}Ti_{18.6}Hf_{28.5} [53] for 650 °C 10h gives a volume fraction of 14.1% which is much closer to the 3-D measured value. However, as with the current literature, the variation of precipitate composition with heat treatments is not known accurately, hence Ni_{53.62}Ti_{20.03}Hf_{26.35} [28] is used.

5.2. Shape of precipitates from 2-D TEMs

The aspect ratio (AR) required for creating ellipsoidal RVEs was estimated from the 2-D TEM images (Fig. 1) by selecting points

Table 1 Summary of volume fractions (VF) calculated from TTs versus from 3-D microstructures in $Ni_{50.3}Ti_{29.7}Hf_{20}[A]$ heat treatment cases. The aspect ratios (AR) of precipitates estimated from 2-D images and 3-D reconstructions are compared with confidence interval (CI).

Heat treatment	Calculated VF	3-D TEM VF	2-D TEM AR AR±(95% CI)	3-D morphology ARs $(AR_1, AR_2)\pm(95\% \text{ CI})$
550°C for 10 h	7.2%	8.5%	2.4 ± 0.5	$(3.1, 1.5) \pm (1.6, 0.8)$
600°C for 10 h	9.2%	9.8%	2.2 ± 0.3	$(2.5, 1.5) \pm (1.2, 0.6)$
650°C for 10 h	9.7%	12.9%	4.2 ± 2.2	$(3.2, 1.8) \pm (1.6, 0.8)$

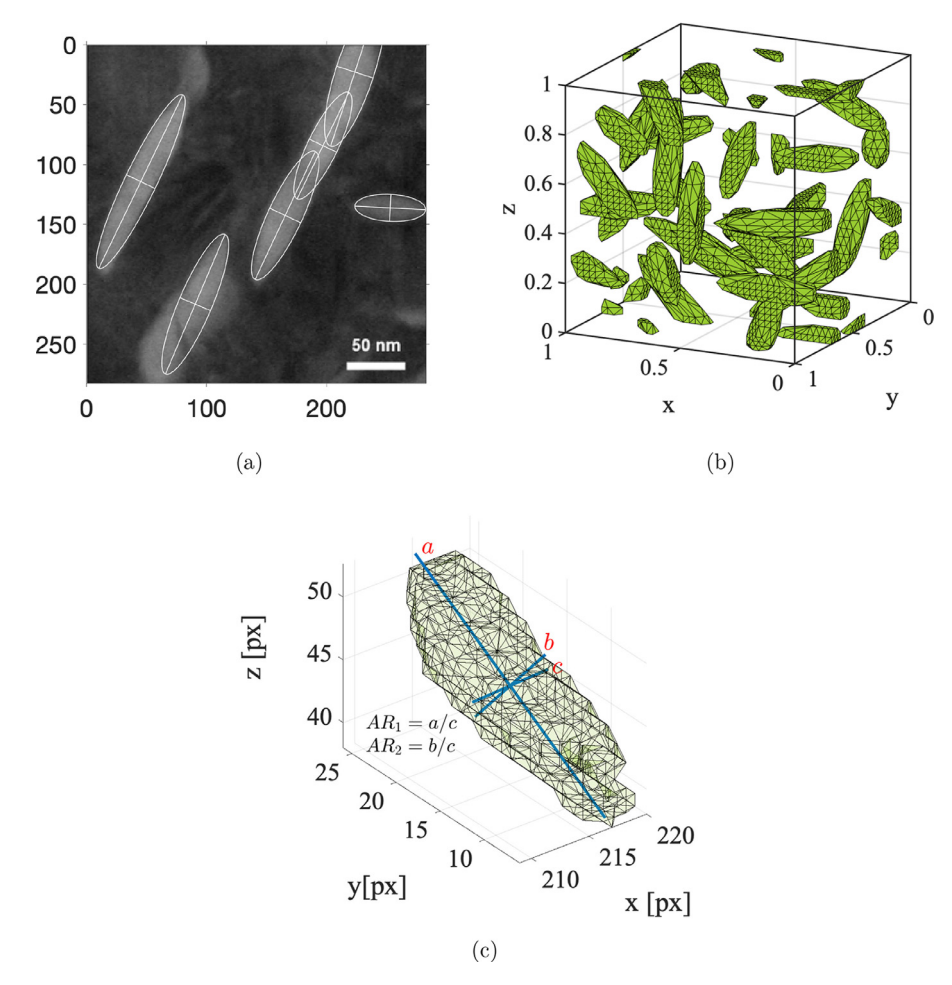


Fig. 9. (a) Calculation of aspect ratio from TEM image in 650 °C 10h sample. (b) An RVE with periodic boundary conditions generated for 650 °C 10h case with 30 particles.(c) Measuring 2 aspect ratios from 3-D reconstruction of an individual precipitate in 650 °C 10h case.

of precipitate boundary and fitting an ellipse using fit_ellipse [67] tool. The schematic in Fig. 9(a) show the calculation performed for the 650 °C 10h sample. The values obtained for different heat treatments are summarized in Table 1. The values of aspect ratios from 3-D reconstruction precipitate morphology by fitting ellipsoids (see Fig. 9(c)) are also compared in Table 1. The single AR values obtained using 2-D TEM images are close to the larger AR in the 3-D shapes. The second AR estimations in the 3-D shapes are close to 1.5, which means the shapes are in fact significantly tri-axial ellipsoidal, whereas in the 2-D TEM based modeling they are assumed to be spheroids with 2 equal axes.

5.3. Generating ellipsoidal RVEs and simulation of behavior

The RVEs of the material were constructed with the calculated volume fraction and aspect ratio (Sections 5.1 and 5.2). Based on

the volume fraction and the number of particles to be modeled, the geometrical dimensions of the individual ellipsoidal particles were determined. Inside the RVE, the ellipsoidal particles were placed at random positions and random orientation. The particles intersecting the faces of the RVE are repeated at the opposite faces to create periodicity and be consistent with periodic boundary conditions. By choosing the random orientations, the cumulative effect from many precipitate orientations in a polycrystal is assumed to be simulated. Measuring the texture of polycrystalline NiTiHf high temperature SMAs is challenging, since heating the sample to the austenitic state requires specialized facilities. Because of this limitation, the crystallographic texture was modeled to be random in the current work. Although within a grain, precipitates can have preferred orientations [68,69], as the grains can be oriented in many directions, the polycrystal will have precipitates in several orientations. The position and orientation of precipitates were determined using a script, which also ensured their period-

icity at the faces. A minimum distance of 1/4 major axis length between the precipitates ensured there were no overlapping particles or particles that were too close to one another. Fig. 9(b) shows an RVE generated corresponding to the 650 °C 10h sample from the TEM in Fig. 9(a).

The steps followed after the RVE creation were the same as described in sections 4 and are not repeated here. The material behavior was predicted from the RVEs by applying periodic boundary conditions and thermo-mechanical loading corresponding to actuation.

6. Estimation of material parameters

The material parameters in the micromechanical model were obtained from available experimental measurements and through calibration with the model.

6.1. Solutionized material composition

In the tension samples of solutionized NiTiHf SMA, the nominal composition was given as $Ni_{50.3}Ti_{29.7}Hf_{20}$ by the manufacturer. However, this may not be the actual composition of the material due to the losses during processing, as described in detail in [70]. While EDX and WDS were two available techniques to measure the composition of the alloy, due to the high sensitivity of TTs to composition in NiTiHf SMAs, the uncertainty in these techniques were considerable from the modeling perspective. Hence, the compositions were estimated from the C-TT relations using the method described in Section 5.1, ensuring the compositions were consistent with the DSC data used in estimating matrix transformation temperatures. For the alloy $Ni_{50.78}Ti_{29.74}Hf_{20}$, the estimated composition of the material (C_0) was $Ni_{50.78}Ti_{29.74}Hf_{19.48}$.

6.2. Properties of the phase transforming matrix

The material parameters in the constitutive model [46] for the matrix which includes TTs (M_s, M_f, A_s, A_f) , phase-diagram slopes (C^A, C^M) , stiffness properties (E^A, E^M) , Poisson's ratio (v^A, v^M) , thermal expansion coefficients (α^A, α^M) and parameters to describe transformation strain variation with stress (H^{\max}, k) , were determined as follows.

6.2.1. Transformation temperatures of the matrix

The TTs for the matrix were calculated from the composition of the matrix (Section 4.3) using the C-TT relations (Section 5.1). For RVEs from 3-D reconstruction, the matrix composition were calculated from their measured VF using Eq. (1). Hence, in TEM RVEs, the dispersion in the VF from different realizations were reflected in the estimations of TTs and consequently in the effective response, while in the ellipsoid RVEs, the matrix compositions were calculated from DSCs (Section 5.1) and had fixed value.

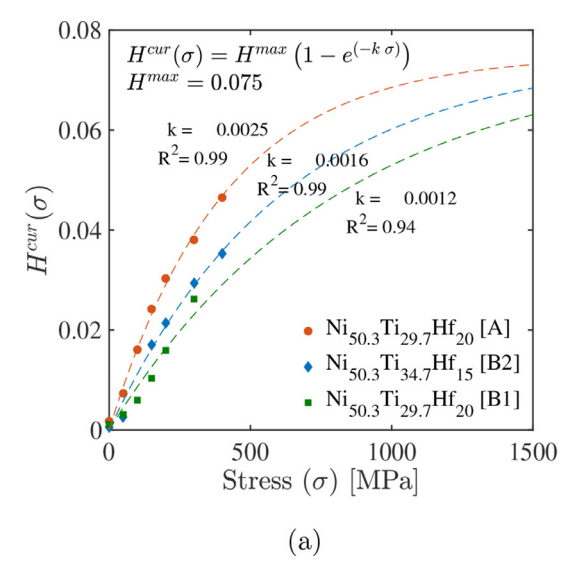
6.2.2. Composition effects on transformation strain and its calibration. The externally measured transformation strain in an SMA can be influenced by its composition, texture, and grain size [70,71]. Regarding the composition effect, the Hf and Ni content can modify the externally measured transformation strain by affecting twin modes and ease of detwinning. The crystallographic calculations in NiTiHf single crystals [71] shows that the Hf content increases the transformation strain. In the same study [71], crystallographic calculations for polycrystal Ni_{50.5}Ti_{36.2}Hf_{13.3} and Ni_{51.2}Ti_{23.4}Hf_{25.4} SMAs show, by increasing Ni (by 0.7%) and Hf (by 12%) content, the transformation strain is decreased (from 4% to 7%). This shows that the Ni content has higher sensitivity, and increasing Ni content reduces the externally measured transformation strain. The difference in texture in SMAs can be caused by a difference in their

processing history, and can affect the transformation strain. When comparing the transformation behavior in solutionized SMAs, the composition and textural effects will be the dominant effects and the grain size effect might be negligible.

In Fig. 10(a), a comparison of experimentally measured transformation strain versus applied load variation in three different solutionized NiTiHf SMAs is shown. Here, the material Ni_{50.3}Ti_{29.7}Hf₂₀ [A] represents the alloy presented in the current work (sections 2 and 3), which was acquired from the company ATI. The materials Ni_{50.3}Ti_{29.7}Hf₂₀ [B1] and Ni_{50.3}Ti_{34.7}Hf₁₅ [B2] represent alloys manufactured in a NASA facility, and the response data is taken from the work of Evirgen [48]. The key difference between [A] and [B] is their processing history. The material [A] was manufactured through a hot forging process, whereas the materials [B1] and [B2] were manufactured through a hot extrusion process. Because of differences in processing, there can be differences in their grain textures, although the composition is the same (in [A] and [B1]). As the two compositions [B1] and [B2] have the same processing history, the texture effects may be negligible, and the difference seen in their externally measured strain can be rationalized solely due to the composition effect. While [A] might be expected to have a lower externally measured transformation strain based solely on composition effect, similar to [B1], the reason for the unexpected difference may be due to the texture effect, i.e., the austenite texture. Because of facilities limitations for measuring the austenite texture, a study on texture was not performed.

The evolution of maximum current transformation strain $(H^{cur}(\sigma))$ with stress can be modeled using an exponential function (shown in Fig. 10(a)) in terms of maximum attainable transformation strain (H^{max}) and an exponent parameter (k). In Fig. 10(a), this variation with stress is fitted to the experimental values in [A], [B1] and [B2], which are shown with the dashed lines. For the three materials, the H^{max} was fixed (= 0.075) and the value of the exponent k was varied, which provided fits with goodness > 0.94. In these measurements, the $H^{cur}(\sigma)$ does not approach saturation before the samples fail in tension at stresses above 400 MPa, so any variation in H^{max} could not be verified. Hence, the strain variations were captured solely through variation in k while assuming fixed H^{max} . The $H^{cur}(\sigma)$ variation in Ni_{50.3}Ti_{29.7}Hf₂₀[A] was verified from responses in four samples, and a comparison of the confidence interval (CI) to the fit is shown in Fig. 10(b). The sample-tosample variation was observed to be less, and the fit matches well with the $H^{cur}(\sigma)$ values generated from measurements on multiple samples.

In addition to the stress variation of transformation strain, the composition variation of transformation strain should be accounted as this is significant in the precipitation hardened behavior (Section 3). Fig. 11 shows a comparison of actuation response predictions in material [A] when the composition effects on transformation strain were not considered in the modeling. Shifts in experimental curves of solutionized sample versus aged sample show clearly how the compositional changes affect both transformation strain and transformation temperature. In the modeling predictions compared in Fig. 11, the composition effect on transformation temperatures, which was well documented (Fig. 8), was included, whereas the $H^{cur}(\sigma)$ was assumed to be the same as the solutionized. The resulting predictions provide for much lower transformation strain compared to the experimental measurements. The difference also increases with volume fraction between heat treatments at 550°C and at 650°C. This increasing difference is due to the increasing k parameter in the matrix with the Ni-lean composition, which should be accounted for in the modeling. Moreover, in Fig. 11, for the same volume fraction, the predictions of ellipsoidal RVEs match well with that of TEM reconstruction RVEs, which shows that the effect of volume fraction through composition is the dominating factor over the geometrical topology.



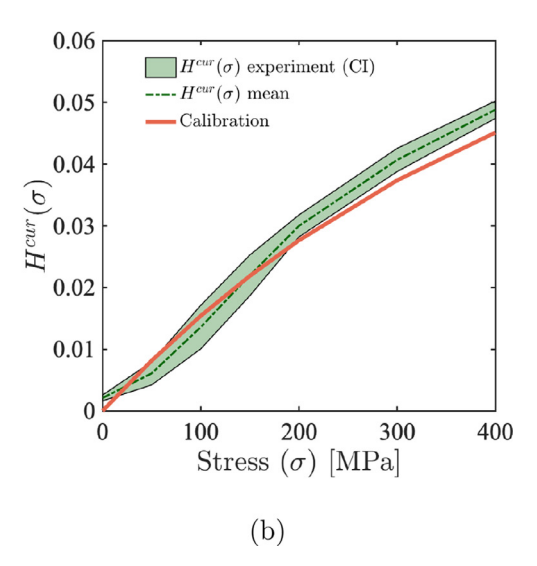
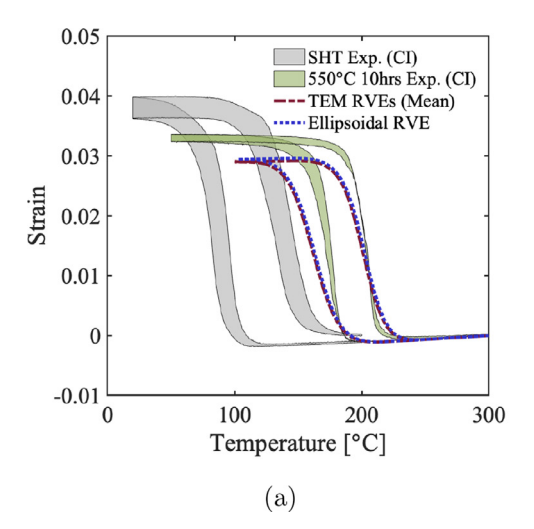


Fig. 10. (a) Experimentally measured stress (σ) dependency of the maximum current transformation strain ($H^{cur}(\sigma)$) in three different solutionized NiTiHf SMAs. (b) Confidence interval (CI) of $H^{cur}(\sigma)$ versus σ generated from experiments performed on four samples of solutionized Ni_{50.3}Ti_{29.7}Hf₂₀[A]. The exponential model for the evolution is fitted to the experimental variation.



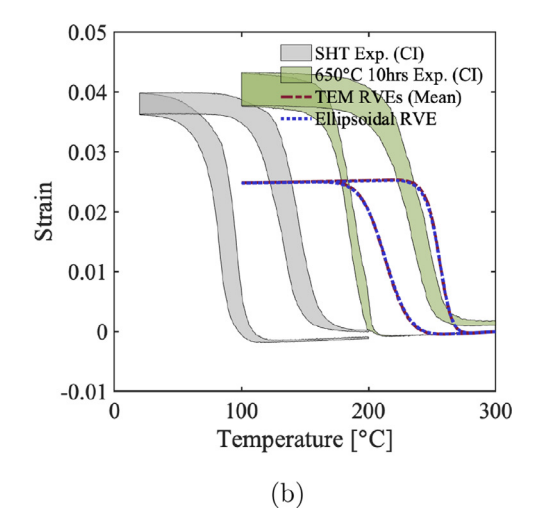


Fig. 11. Comparison of micromechanical prediction for actuation response at 300 MPa using a TEM RVE neglecting the compositional effects of k in precipitation hardened Ni_{50.3}Ti_{29.7}Hf₂₀[A] heat treated at (a) 550°C for 10h and (b) 650°C for 10h. Prediction from an ellipsoidal RVE with same volume fraction is shown. For the TEM case, the mean value from the two in-plane loading directions is shown.

With the knowledge that the parameter k and Ni composition are inversely related, k for additional Ni compositions were calibrated from the heat-treated responses using the micromechanical model simulations. Fig. 12 shows the variation of k obtained for the three alloys, where the values obtained from the solutionized experiments ('Expt.') and values from the aged response ('Calibration') are correlated with Ni composition. For [A], two heat treatment response (550 °C 10h and 650° 10h at 300 MPa) were used in the calibration and a spline interpolation was used. For [B1], one heat treatment response (550 °C 3h at 300 MPa) was used for calibration with linear interpolation. Similarly, for [B2], one heat treatment response (600 $^{\circ}\text{C}$ 10h at 300 MPa) was used for calibration with linear interpolation. The higher values in the [A] alloy compared to the ([B1] and [B2]) alloys can be explained as the result of differences in texture due to different processing history. Compared to [A], the alloys [B1] and [B2] give closer values, probably due to similar texture in both. As the variation of k in a wide range of composition was captured, the matrix can now be modeled with composition effects on transformation strain.

6.2.3. Calibration of remaining properties

The properties such as: phase-diagram slopes (C^A , C^M), stiffness (E^A , E^M), Poisson's ratio (v^A , v^M) and thermal expansion coefficients (α^A , α^M) were assumed to be constant with composition. The values for these parameters were obtained from calibration of solutionized SMA actuation response with the Lagoudas et al. constitutive model following the standard methodology in [46]. Table 2 shows the summary of the calibrated values in the phase diagram and other parameters in the model.

Fig. 13 shows a comparison of the experimental and the calibrated model phase diagrams for the solutionized Ni_{50.3}Ti_{29.7}Hf₂₀ SMA, where the transformation temperatures at each stress level were estimated from the actuation responses using the tangent approach (Section 3). For the experimental phase diagram in Fig. 13, the discrepancy between different samples of Ni_{50.3}Ti_{29.7}Hf₂₀ is shown as a confidence interval of one standard deviation. As the nonlinear variation in the phase diagram of NiTiHf could not be captured exactly in the SMA constitutive model, the phase diagram curves were approximated in the modeling with the solid curves illustrated in Fig. 13. In Fig. 14, comparison of experimen-

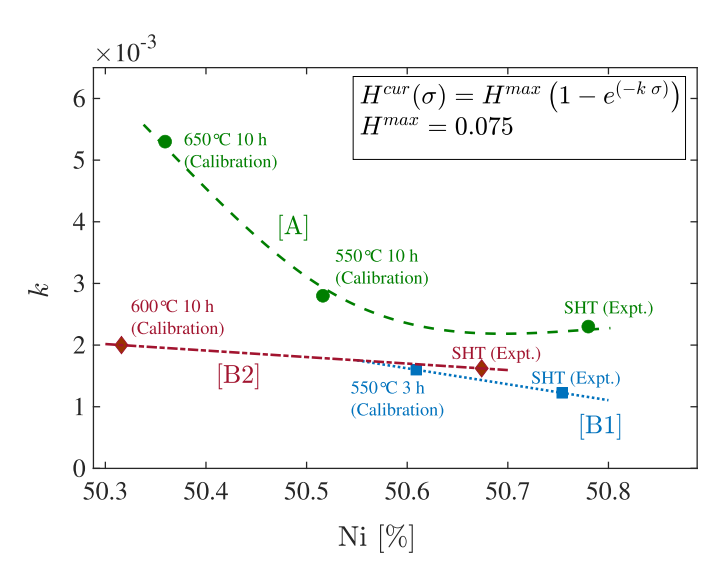


Fig. 12. Variation of exponent k in solutionized NiTiHf alloys with Ni composition for three different alloys, where [A] (alloy in this work) and ([B1], [B2]) [48] have different processing parameters. The curves were developed using points from experimental measurements (Expt.) and values estimated through calibration with the micromechanical model.

tal and the calibrated constitutive model responses in solutionized $Ni_{50.3}Ti_{29.7}Hf_{20}$ SMA for 200 MPa and 300 MPa is shown, where the CI is used to represent variation from four different samples. The experiment curves and the calibrated model curves have a matching response, indicating the parameters to be appropriately estimated.

Following are some of the intrinsic assumptions that have been made in this estimation of parameters.

- 1. The grain morphology of the solutionized SMA and the precipitation-hardened SMA samples were assumed to be the same. Although the grain boundaries can grow during aging, this change in grain morphology is usually minimal, since the growth kinetics at aging temperatures (500 °C 700 °C) are much slower than that at the solutionizing temperature (1000 °C). With this assumption, the changes in the matrix properties due to grain morphology changes in the aging were disregarded.
- 2. It was shown in the previous sections that the matrix composition changes with volume fraction. By assuming fixed model

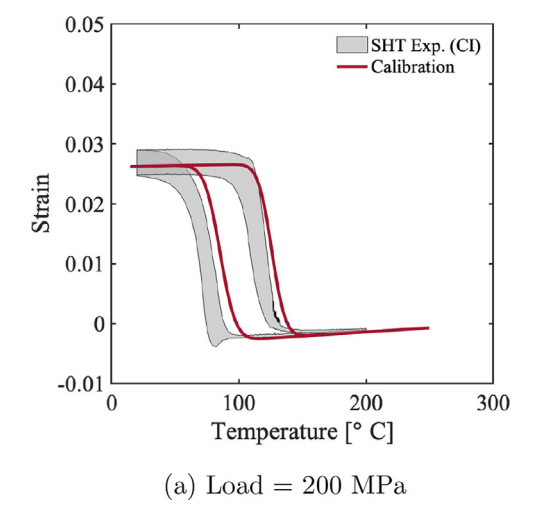


Table 2SMA properties obtained for solutionized Ni_{50.3}Ti_{29.7}Hf₂₀[A] through calibration of experimental responses using Lagoudas et al. [46] constitutive model.

Material parameter	Value
E_A	79 GPa
E_M	83 GPa
α^A	$1.38 * 10^{-5}$
α^{M}	$4.34 * 10^{-6}$
$v^{A} = v^{M}$	0.4
H ^{max}	0.075
$k[MPa^{-1}]$	0.00267
C_A	8 MPa/K
C_M	13 MPa/K
$n_1 = n \ldots = n_4$	0.1

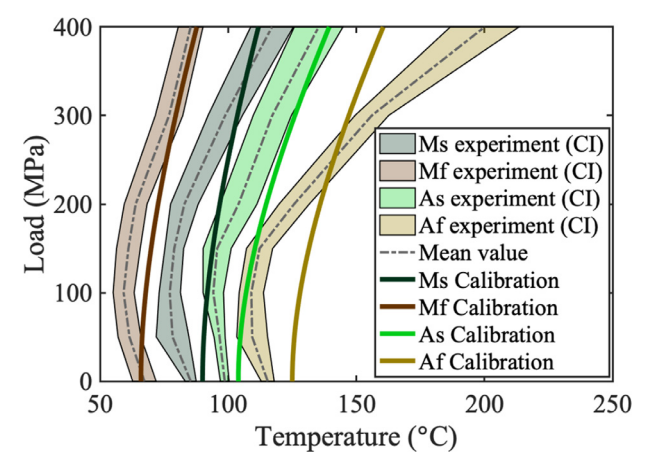


Fig. 13. The temperature-stress phase diagram for $Ni_{50.3}Ti_{29.7}Hf_{20}[A]$ developed from experimental responses in four samples presented with confidence interval (CI). The phase diagram from the calibration of Lagoudas et al. [46] constitutive model is compared.

parameters after different aging heat treatments, the influence of composition changes on these properties were disregarded.

6.3. Estimation of precipitate phase stiffness

The precipitate phase is expected to be stiffer than the solutionized phase, so the aged SMA will be stiffer than the solution-

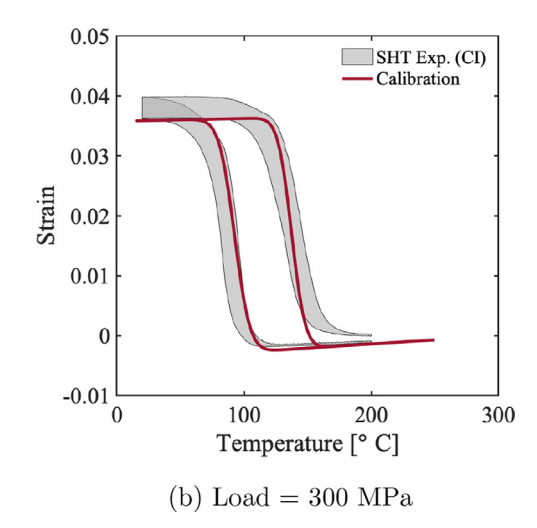


Fig. 14. Comparison of the Lagoudas et al. [46] model responses to the experimental responses for the solutionized Ni_{50.3}Ti_{29.7}Hf₂₀[A] at (a) 200 MPa and (b) 300 MPa.

Table 3 Austenite phase stiffness values for different heat treatments in $Ni_{50.3}Ti_{29.7}Hf_{20}[A]$ and their estimated values from the finite element micromechanical model.

Material aging	Experimental Young's modulus (GPa)	Value from E_P estimation (GPa)
Solutionized	79.6 ± 2.4	-
550°C for 10 h	80.8 ± 1.8	80.6 ± 2.1
600 °C for 10 h	82.2 ± 2.7	80.8 ± 2.1
650°C for 10 h	84.4 ± 4.1	81.3 ± 2.0

ized SMA. As the RVEs of the aged SMAs were known from the TEM reconstructions, the precipitate stiffness could be calibrated from the higher stiffness values in the aged samples, assuming matrix stiffness to be the same as in the solutionized. The micromechanical model was used to calibrate the precipitate stiffness from the austenite stiffness values of the solutionized and three heat-treated SMA samples. Experimental stress-strain values above 300°C, where the material is expected to be fully in the austenite phase, were used to estimate the austenite stiffness values. These values are summarized in Table 3 with the mean and bounds reflecting standard deviation of sample-to-sample discrepancy from several samples (3–4).

With the solutionized material stiffness (E_{sht}) in the matrix, the effective stiffness of the RVEs were estimated in the micromechanical model for different precipitate stiffness (E_P) values. Considering the uncertainty from multiple samples, the precipitate stiffness was estimated using maximum likelihood estimation (MLE), which allowed accounting for these uncertainties in the estimation. The following equations summarize the likelihood function(\mathcal{L}) estimation for the precipitate stiffness (E_P).

$$\mathcal{L}(E_P) = \prod_{Ag=1,2,3} \mathcal{L}(E_P|Ag),$$

$$\mathcal{L}(E_P|Ag) = \int_{-\infty}^{\infty} \mathcal{L}(E_P|E_{Ag}) \mathcal{L}(E_{Ag}) dE_{Ag},$$
(3)

where, Ag = 1, 2, 3 represents the three aging conditions corresponding to 550°C, 600°C and 650°C respectively, and E_{Ag} corresponds to the austenite stiffness of the aged SMA. $\mathcal{L}(E_P|E_{Ag})$ represents the likelihood of E_P in the model for a fixed E_{Ag} when accounting for the uncertainty in the solutionized stiffness ($\mathcal{L}(E_{sht})$) and its propagation in the model for estimating the E_{Ag} . The likelihood functions $\mathcal{L}(E_{sht})$ and $\mathcal{L}(E_{Ag})$ were assumed to have Gaussian distributions and were calculated from the experiments using the mean and standard deviation reported in Table 3. The analysis gave E_P to be 95 ± 26 GPa based on the MLE, and this value was used in the further analysis. Table 3 also compares the estimations from MLE with the experiments. The calibrated stiffness in the 550°C case is close to the experimental value owing to its higher precision across samples. The 600°C and 650°C cases, because they had lower precision across samples, contributed less to the calibration of E_P . In conclusion, better precision measurements contribute more to the maximum likelihood estimation, while observations with substantial uncertainties contribute less.

7. Results and discussion

The developed micromechanical modeling framework was used to model the precipitation hardened responses in Ni_{50.3}Ti_{29.7}Hf₂₀ [A], Ni_{50.3}Ti_{29.7}Hf₂₀ [B1] and Ni_{50.3}Ti_{34.7}Hf₁₅ [B2] SMAs for different heat treatment conditions. For aged [A] SMAs the modeling was performed using TEM reconstruction RVEs (Section 4) and ellipsoidal RVEs (Section 5). For [B1] and [B2] SMAs, the precipitation hardened responses were modeled using the ellipsoidal RVEs

and comparisons were made with experimental responses available in the literature [48].

7.1. Predictions of responses in precipitation hardened $Ni_{50.3}Ti_{29.7}Hf_{20}$ [A] SMA

Figs. 15, 16 and 17 show predictions of actuation responses in [A] for heat treatment conditions 550°C 10h, 600°C 10h and 650°C 10h respectively. The experimental responses of solutionized (SHT) and heat treated SMAs are shown along with the modeling. Because of the sample-to-sample variation, the experimental responses are presented with confidence intervals (Cls) of 1 standard deviation accounting for differences from many samples (3 for SHT, 2 for 550°C, 2 for 600°C and 3 for 650°C). The predicted responses from four TEM RVEs are also shown with confidence interval(Cl) with their mean response. For the predictions from the ellipsoidal RVE, a single response is shown, since there was little variation between different realizations.

Depending upon on the extent of spatial variation of volume fraction in the 3-D TEM reconstruction, the predictions using the four TEM RVEs gave wider confidence regions in the responses. In 550°C , we see 3-D reconstruction to be uniform with little spatial variation of volume fraction $(8.5\pm0.3\%)$, and the predictions also showed tight confidence intervals, whereas in 600°C , the TEM RVEs responses gave wider CI, mainly due to the higher spatial variation of volume fraction $(9.8\pm3\%)$. At 650°C as well, the responses from TEM RVEs had wider confidence interval because of the higher spatial variation in the volume fraction $(12.9\pm2.5\%)$. The irregular transformation shapes in the mean response shown in the Fig. 16 are only an artifact from the spread of responses in different realizations. Also, the peaks in the confidence interval for the case of 600°C at 300 MPa and 650°C are produced when there is large scatter along temperatures, which can also be seen in [72].

In the comparisons shown (Figs. 15-17), an increase in transformation strain with increasing precipitation was observed in the three aging conditions. In the 550°C heat treatment compared to the solutionized, the responses give comparable strain at lower stresses (100 MPa and 200 MPa) and lower strain at high stress (300 MPa), while in the 600°C heat treatment, strain values are higher at lower stresses (100 MPa,200 MPa) and comparable at high stress (300 MPa) to the solutionized responses. In the 650° heat treatment, higher strain values were seen compared to the solutionized SMA at all stress levels. This increasing behavior on strain with precipitation is explained using the compositional effects on transformation strain (Section 6.2.2). As the extent of precipitation increased from 550°C to 650° heat treatment, the transformation strain ($H^{cur}(\sigma)$) in the matrix increased due to the composition effect, and this resulted in the observed gradual increase of strain in these heat treatments. With the composition effect on transformation strains accounted for, the model is able to predict the rise in transformation. Although the heat treatment 600°C was not used in the calibration, the close prediction of strain values validates the composition variation in Fig. 12. This shows the ability of the developed micromechanical model to predict the transformation strain in new heat treatments.

The temperature ranges of transformation predicted in the responses of TEM RVEs and ellipsoidal RVEs are close to the experimental measurements (see Figs. 15–17). The Ellipsoidal RVEs gave slightly lower temperature range compared to the TEM RVEs due to the lower volume fraction estimations in the methodology (see Table 4). As the volume fraction of precipitates increases, the matrix becomes more Ni-lean and the transformation temperatures increase with the Ni-lean matrix. The good agreement between the predictions from micromechanical modeling with experimental measurements shows that the method of microstructure reconstruction from TEM images provides volume fraction values in the

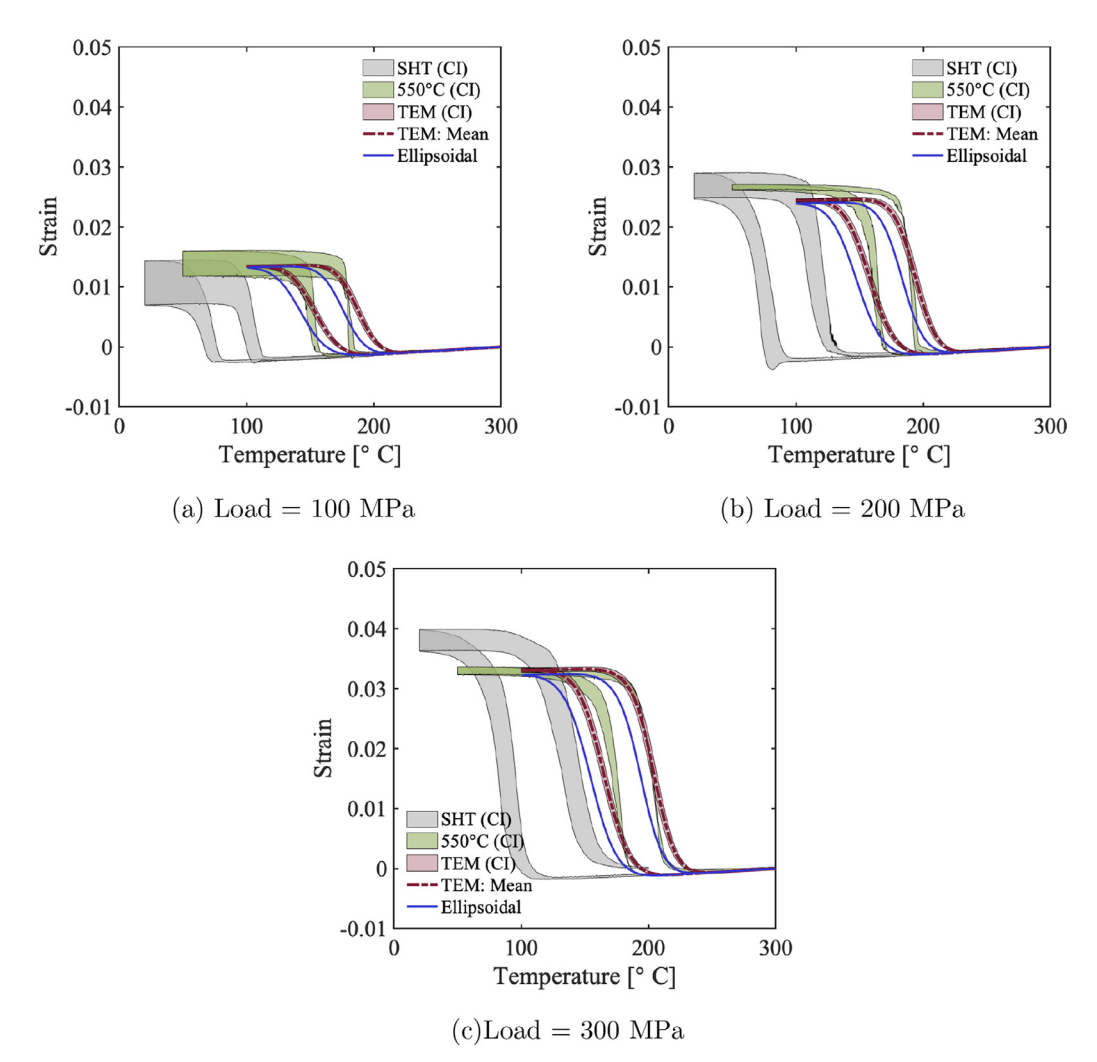


Fig. 15. Comparison of predictions to experimental responses in $Ni_{50.3}Ti_{29.7}Hf_{20}$ [A] aged at 550 °C for 10h. The experimental responses of solutionized material (SHT) and the heat treated material (550 °C) from different samples are presented with confidence interval (CI). The predictions from four TEM RVEs are presented with CI and prediction from ellipsoidal RVE is compared.

Summary of volume fraction (VF) and aspect ratio (AR) estimations in precipitation hardened $Ni_{50.3}Ti_{34.7}Hf_{15}[B2]$ and $Ni_{50.3}Ti_{29.7}Hf_{20}[B1]$ SMAs.

SHT material & calculated composition	Heat treatment	Aged material [Ms Mf As Af]	Calculated VF	AR
$\begin{array}{l} Ni_{50.3}Ti_{34.7}Hf_{15}[B2]\\ (Ni-50.67,Hf-15)\\ Ni_{50.3}Ti_{29.7}Hf_{20}[B1]\\ (Ni-50.75,Hf-20) \end{array}$	550 °C for 3h	[46 37 91 102]	0.038	3 ± 0.5
	600 °C for 10h	[109 65 113 170]	0.107	5 ± 0.5
	500 °C for 48h	[150 130 162 177]	0.045	2.5 ± 0.5
	550 °C for 3h	[155 128 160 181]	0.047	2.7 ± 0.5

realistic range. The ellipsoidal RVE methodology produced comparable predictions for all heat treatments and stress levels, which indicates it is a good methodology for RVEs in new materials and also gives volume fractions in a realistic range.

7.2. Prediction in SMAs with different processing parameters

The developed micromechanical modeling framework was implemented to study the HTSMAs with a different processing history. The RVE based on ellipsoidal methodology (Section 5) was used for modeling the precipitation hardened responses in $Ni_{50.3}Ti_{34.7}Hf_{15}[B2]$ and $Ni_{50.3}Ti_{29.7}Hf_{20}[B1]$ SMAs from the work by Evirgen [48]. The summary of the estimated composition, volume fraction and aspect ratios is given in Table 4. The variation of k with composition from Fig. 12 was used. The additional material parameters for the SMA matrix were assumed to be the same

as Table 2. Responses of material [B2] in two heat treatment conditions (550 $^{\circ}$ C 3h and 600 $^{\circ}$ C 10h) were modeled. Similarly, for material [B1], two heat treatment (500 $^{\circ}$ C 48h and 550 $^{\circ}$ C 3h) responses were modeled.

Fig. 18 and Fig. 19 show the actuation response comparisons in [B2] and [B1] respectively. The response at 200 MPa and 300 MPa were predicted using the micromechanical model for different heat treatment cases, and are compared with experimental responses of solutionized and aged SMAs. The heat treatment cases 550 °C for 3h in [B2] and 500 °C for 48h in [B1] were not used in the calibration, but predicted well with the developed model. The comparisons (Fig. 18(a) and (b), Fig. 19 (a) and (b)) show that the model is able to predict the strain values and the temperatures of transformation close to the experiments in these new heat treatments.

In the aged [B2] SMAs experiments (Fig. 18), a higher value of maximum strain is observed in 550 °C for 3h and a lower value

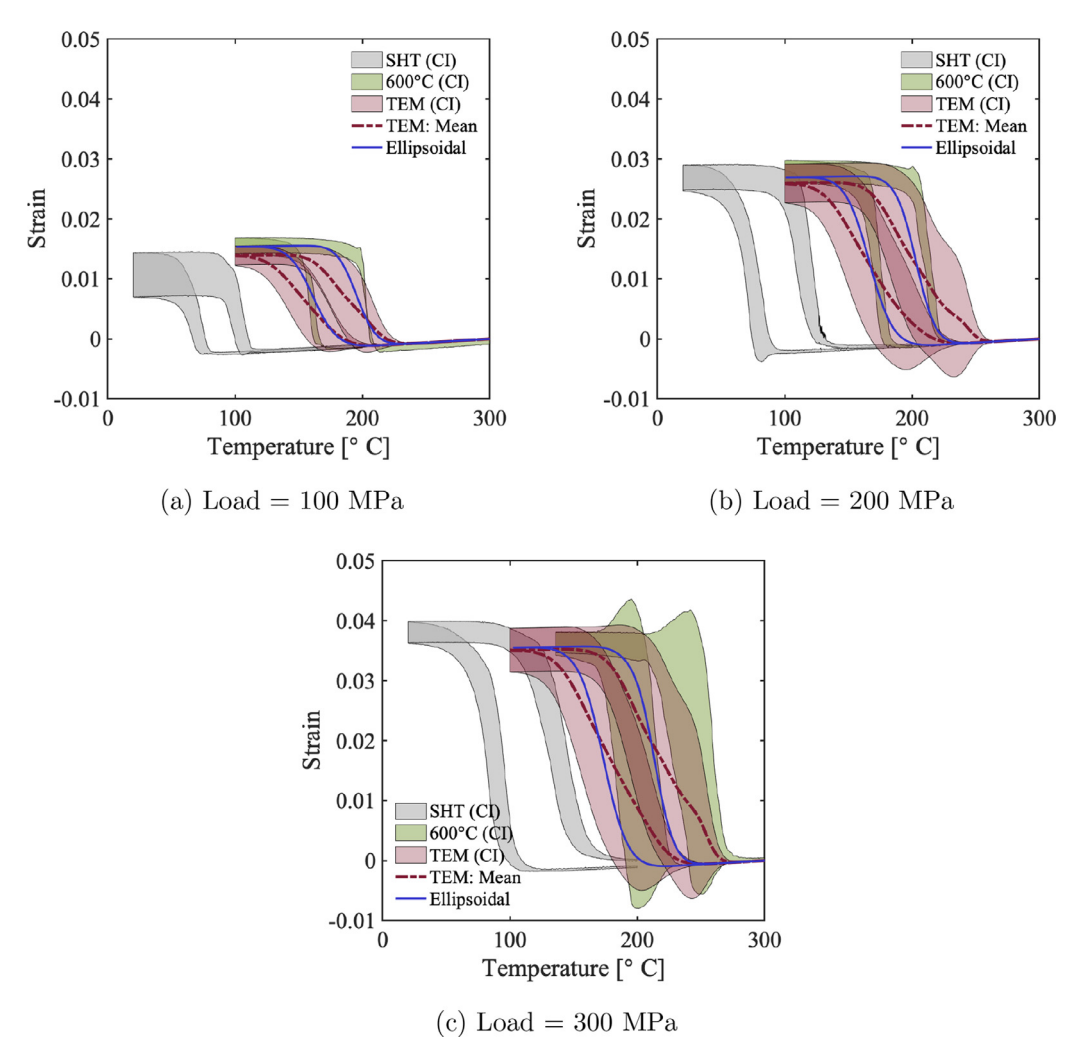


Fig. 16. Comparison of predictions to experimental responses for $Ni_{50.3}Ti_{29.7}Hf_{20}$ [A] aged at 600 °C for 10h. The experimental responses of solutionized material (SHT) and the heat treated material (600 °C) from different samples are presented with confidence interval (CI). The predictions from four TEM RVEs are presented with CI and prediction from ellipsoidal RVE is compared.

in 600 °C for 10h in comparison with the solutionized. The lower strain in 600 °C for 10h in comparison to the solutionized contrasts with the behaviors seen in the aged [A] SMAs, where higher strain was observed compared to the solutionized with increase in precipitation. Looking into the k variation for [B2] SMAs (Fig. 12), we see a lower gradient with decreasing composition, which indicates a less dominant composition effect of transformation strain in this alloy. Hence, it can be concluded that in 600 °C 10h heat treatment, the constraining effects of precipitates because of a higher volume fraction (= 0.107) dominates over the composition effect resulting in a lower strain, while in 550 °C for 3h, the composition effects dominated and resulted in a higher strain than the solutionized response. The micromechanical modeling is able to capture the trend in the modeling.

In the two heat treatments (500 °C 48h, 550 °C 3h) in [B1] SMA, we see higher strains in both heat treatments compared to the solutionized response. This can be explained by the competing effects of composition change and precipitation hardening. The volume fraction estimation in these heat treatments are $\approx 4.5\%$ (see Table 4), which can be considered to be lower. When examining the composition effect in [B1], it has a stronger gradient of k versus composition than [B2], indicating a stronger composition effect (see Fig. 12). The higher transformation strain in the presented heat treatments of [B1] can be attributed to the stronger composition effect, which dominates over the constraining ef-

fect from precipitates. The modeling successfully captured these higher strains through accounting to the compositing variation of k.

8. Conclusions

This paper presents a study on the phase transformation behavior of precipitation-hardened NiTiHf SMAs, focusing on their micromechanical modeling. The aged NiTiHf SMAs produced higher transformation strain with precipitation, which was counterintuitive, as the non-transforming precipitates would have reduced the phase transformation. Further, investigating the responses of Ni-TiHf SMAs with different compositions and processing, it was observed that the extent of transformation at given stress depends on composition and processing. The higher strain behavior in the precipitation hardened SMAs can be explained by the changing of transformation strain in their matrix with composition.

A finite element based micromechanical model was developed for the precipitation hardened NiTiHf SMAs taking into consideration the composition effects in their matrix phase transformation. Two methods of RVE generation were considered: 1) RVEs based on TEM reconstructions of the aged SMAs and 2) ellipsoidal RVEs with an estimated volume fraction. The modeling framework was implemented to model behavior in NiTiHf SMAs from two different processing methods. The predictions demonstrated good compari-

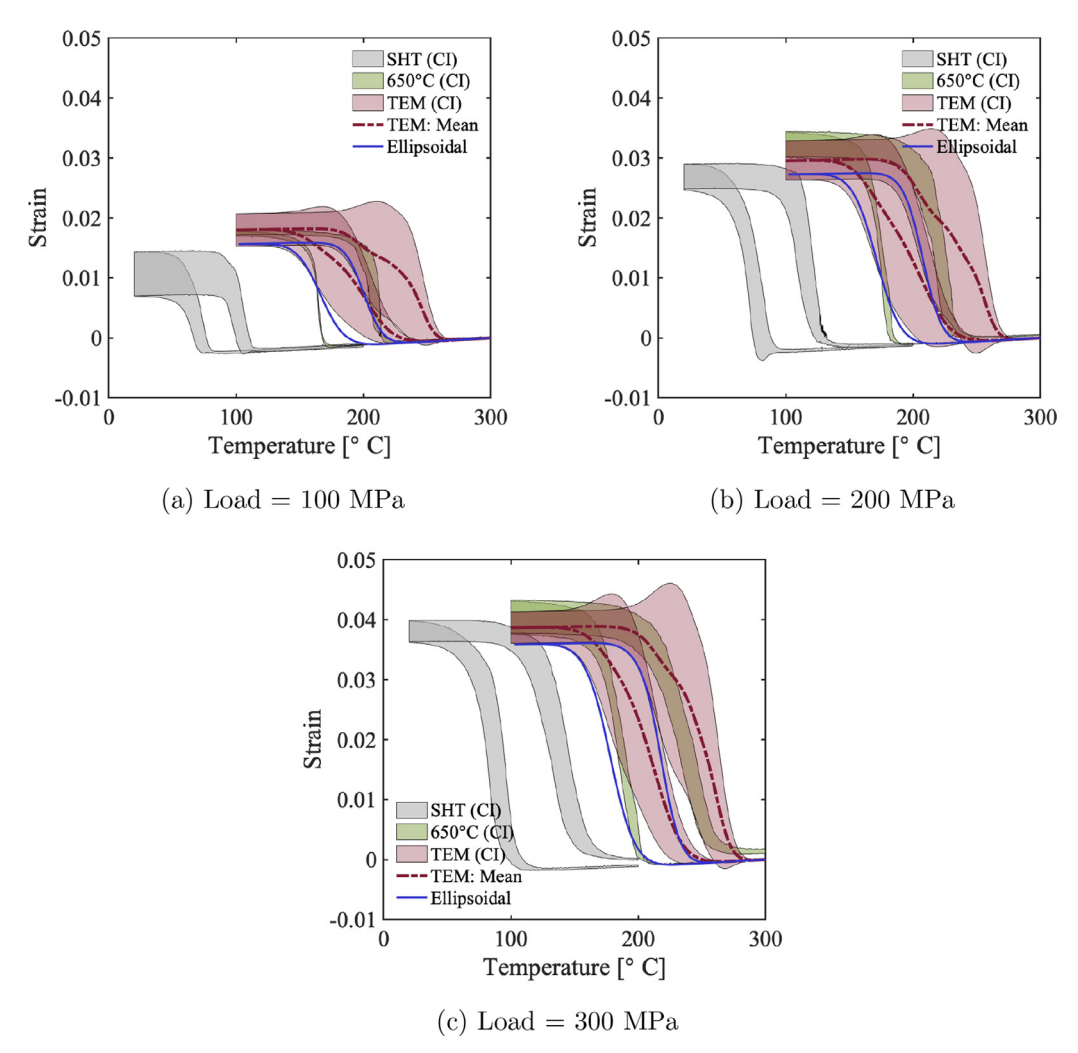


Fig. 17. Comparison of predictions to experimental responses for $Ni_{50.3}Ti_{29.7}Hf_{20}$ [A] aged at 650 °C for 10h. The experimental responses of solutionized material (SHT) and the heat treated material (650 °C) from different samples are presented with confidence interval (CI). The predictions from four TEM RVEs are presented with CI and prediction from ellipsoidal RVE is compared.

son for temperature range of transformation and maximum strain to the experiments. To the best of the authors' knowledge, the present work constitutes the first study of the prediction of the actuation response of high temperature SMAs by considering realistic microstructures in the model.

Following are some key results from the developed micromechanical model.

- 1. The volume fraction in the microstructure was found to be the dominant factor over the exact details of microstructural topology in predicting the behavior.
- Accounting for the composition dependency of transformation strain in the modeling was necessary to capture the increasing strain values in the precipitation-hardened NiTiHf SMA behavior. The model predicted significantly lesser values of strain when the composition dependency was not accounted for.
- Upon incorporating the dependency of the transformation strain on compositional content in the matrix, the model predicts the behavior in accordance with the experimental observations.
- 4. The less expensive methodology of RVE generation based on approximated ellipsoidal predicts the behavior with good agreement with predictions from the RVEs generated based on TEM reconstructions. This provides a rigorous computational framework for heuristic studies in exploring the sensitivity of

- the behavior as a function of several microstructural and compositional parameters.
- 5. The resulting model was employed to study the effects due to processing history on the constitutive behavior of these alloys.

The key implication of this work is that the resulting framework will be useful in optimizing the heat treatment processes to get desired microstructures. As a result, it will be useful in the faster and systematic heat treatment designing in NiTiHf HTSMAs for a specific application.

Declaration of Competing Interest

The authors declare that they have no known competing financial interests or personal relationships that could have appeared to influence the work reported in this paper.

Acknowledgments

This work is supported by Designing Materials to Revolutionize and Engineer our Future (DMREF) Program under National Science Foundation (NSF) under the Award Number: 1534534. Evaluations of the thermo-mechanical behavior were carried out in the Texas A&M Supercomputing Facility. The authors would also like to acknowledge the NSF-DMR grant 2004752. Author acknowledge Dr.

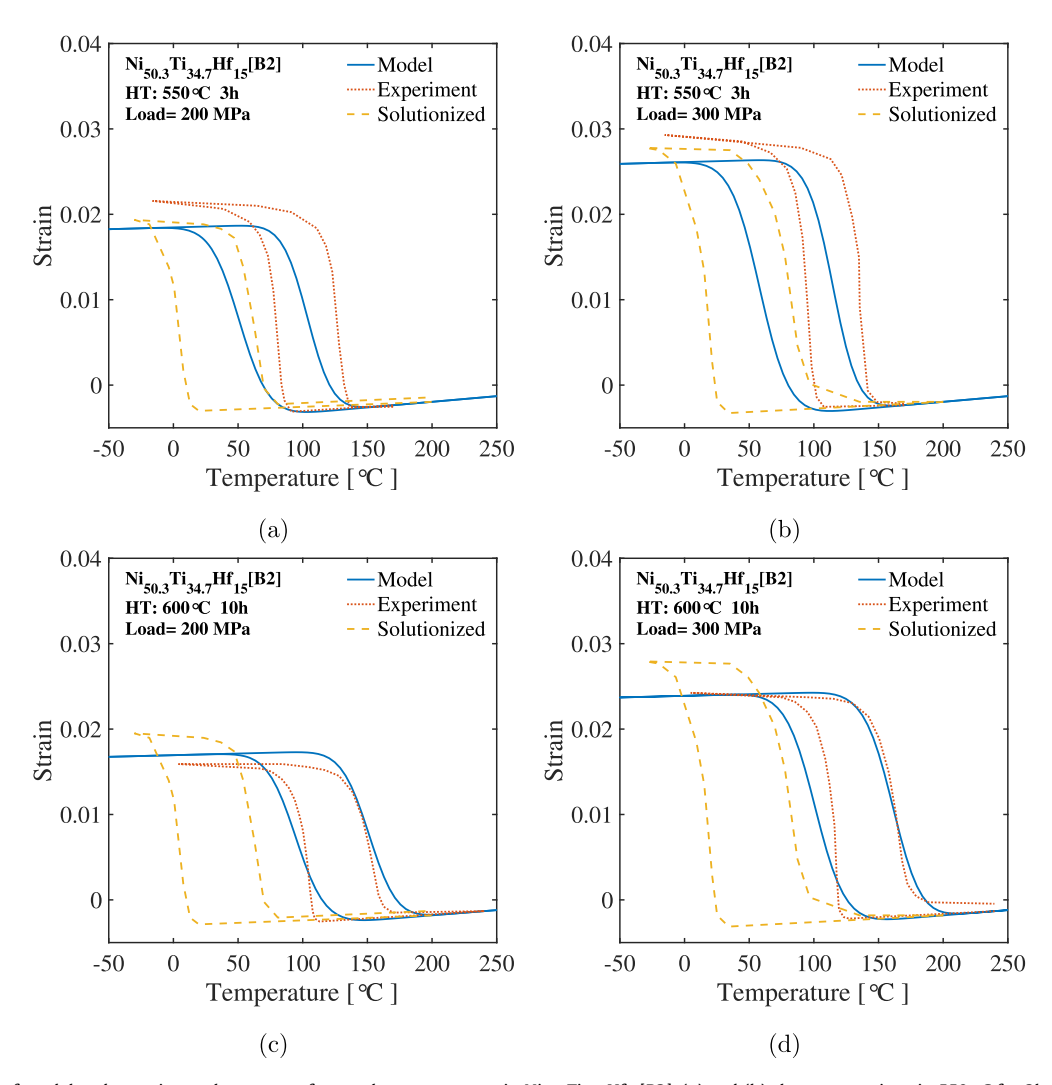


Fig. 18. Comparison of model and experimental responses for two heat treatments in $Ni_{503}Ti_{34.7}Hf_{15}[B2]$. (a) and (b) show comparison in 550 °C for 3h responses at 200 MPa and 300 MPa, (c) and (d) show comparison in 600 °C for 10h responses at 200 MPa and 300 MPa.

Manish Vasoya, Dr.Anargyros Karakalas and Ralston Fernandes for giving feedback on the manuscript, and Chris Mabe for comments on the writing.

Appendix A. Comparison of stiffness calculation in a polycrystal

In this section, the effective stiffness of a precipitationhardened polycrystal was calculated with two different methodologies, and the results were analyzed. Fig. A1 summarizes the RVEs in the two methodologies.

In Case 1 methodology, the effective behavior of the polycrystal was modeled using a multiscale modeling at two levels: inside a grain and between grains. A unit cell with single precipitate and an RVE of polycrystal with many grains were used for modeling inside the grain and the grain interaction respectively. The effective stiffness of the grain was calculated using the unit cell in Fig. A1(a). The unit cell has only single orientation of precipitate to simulate preferred orientation of precipitates in a grain [68,69]. For modeling polycrystal interaction, an RVE with 200 grains was created in open-source DREAM3D software and shown in Fig. A1(a). Random orientations were considered in these 200 grains. The effective stiffness of the polycrystal was calculated from the polycrystal RVE, with the effective stiffness from the unit cell in each grain.

Periodic boundary conditions were used at the boundary of the RVFs

In the Case 2 methodology, the effective stiffness matrix was solved from a single RVE with many precipitates in random position and orientations (shown in Fig. A1(b)). The matrix is assumed to have the properties of a polycrystal without precipitation. Precipitates have the same property as modeled using the unit cell. Through the precipitates in many random position and orientation, the cumulative effect of the precipitates from many grains were simulated. Periodic boundary conditions were used at the boundary of the RVEs.

A1. Stiffness properties of matrix and precipitate

Isotropic stiffness properties were assumed in both cases for the matrix and the precipitates. The stiffness properties were chosen to indicate the upper bound of tangent stiffness during phase transformation. The matrix was chosen to have a softness of an SMA matrix during phase transformation. Considering an upper bound for transformation strain (= 0.2 at 200 MPa) in the SMA matrix, the tangent stiffness in the SMA matrix during phase transformation will be less than 1 GPa. Hence, the matrix in these calculations were assumed to have isotropic linear elastic property with Young's modulus of 1 GPa and Poisson's ratio of 0.4. Similarly, the precipitate stiffness was taken to be in the same order

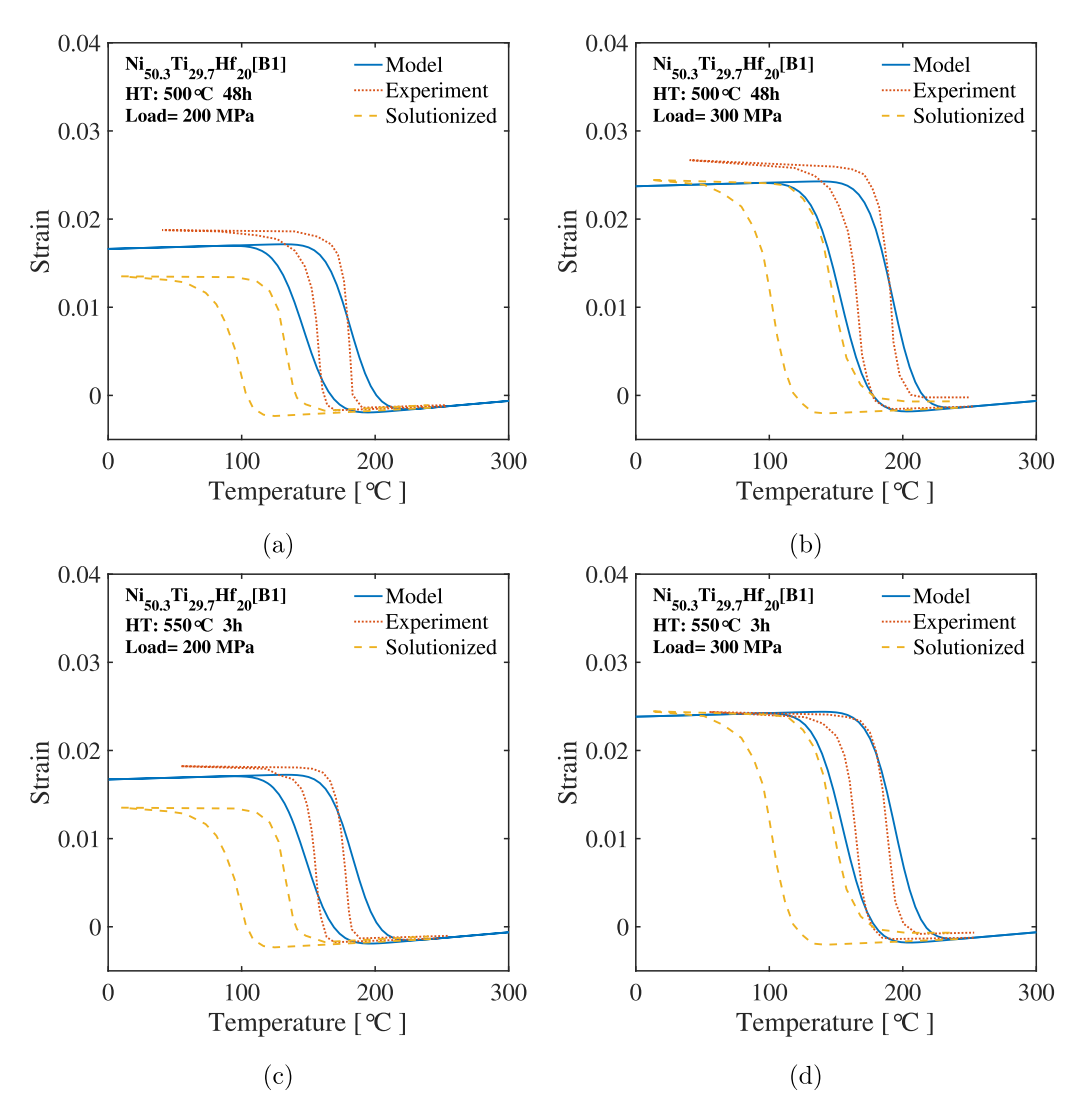


Fig. 19. Comparison of model and experimental responses for two heat treatments in $Ni_{50.3}Ti_{29.7}Hf_{20}[B1]$. (a) and (b) show comparison in 500 °C for 48h responses at 200 MPa and 300 MPa, (c) and (d) show comparison in 550 °C for 3h responses at 200 MPa and 300 MPa.

found in the SMAs. The precipitates were assumed to be isotropic linear elastic with Young's modulus of 100 GPa and Poisson's ratio of 0.4.

A2. Case 1: Multi-scale modeling with two scale calculation

First, the effective stiffness matrix for the grain was solved from the unit cell with precipitates. The calculation was carried out by applying unit load along normal and shear directions, and the stiffness matrix was calculated from the resulting strains produced. The solution was performed using the fast Fourier transform (FFT) algorithm described in the work of Cruzado et al. [73]. The effective anisotropic stiffness matrix of the unit cell ($C_{eff}^{unit\ cell}$) was obtained to be the following.

$$\begin{bmatrix} C_{eff}^{unit\ cell} \end{bmatrix} \approx \begin{bmatrix} 3.76 & 1.84 & 1.82 & 0.01 & -0.04 & -0.13 \\ 1.84 & 2.73 & 1.82 & -0.01 & 0.03 & -0.02 \\ 1.82 & 1.82 & 4.27 & -0.1 & -0.05 & 0 \\ 0.01 & -0.01 & -0.1 & 0.51 & -0.07 & 0.01 \\ -0.04 & 0.03 & -0.05 & -0.07 & 0.91 & -0.04 \\ -0.1 & 0 & 0 & 0 & 0 & 0.5 \end{bmatrix} GPa$$

Second, the effective macroscopic stiffness of the polycrystal was calculated from the polycrystal RVE. The stiffness matrix for each grain was assigned from the unit cell effective stiffness with random rotation. The effective macroscopic stiffness matrix (C_{eff})

was solved applying unit loads along normal and shear directions.

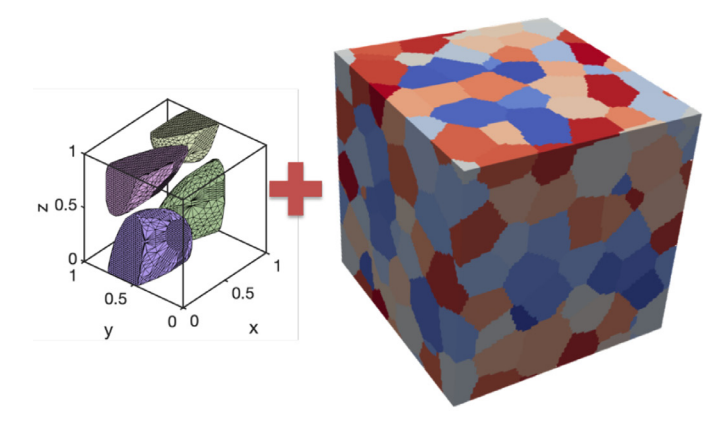
$$\begin{bmatrix} C_{eff} \end{bmatrix} \approx \begin{bmatrix} 3.43 & 1.9 & 1.89 & -0.01 & 0.01 & -0.01 \\ 1.9 & 3.39 & 1.89 & -0.01 & 0 & -0.02 \\ 1.89 & 1.89 & 3.16 & 0 & 0 & 0.02 \\ -0.01 & -0.01 & 0 & 0.76 & -0.01 & 0 \\ 0.01 & 0 & 0 & -0.01 & 0.65 & -0.01 \\ -0.01 & -0.02 & 0.02 & 0 & -0.01 & 0.64 \end{bmatrix} GPa$$

$$\approx C[E = 1.93 \text{ GPa}, \ \nu = 0.36]$$

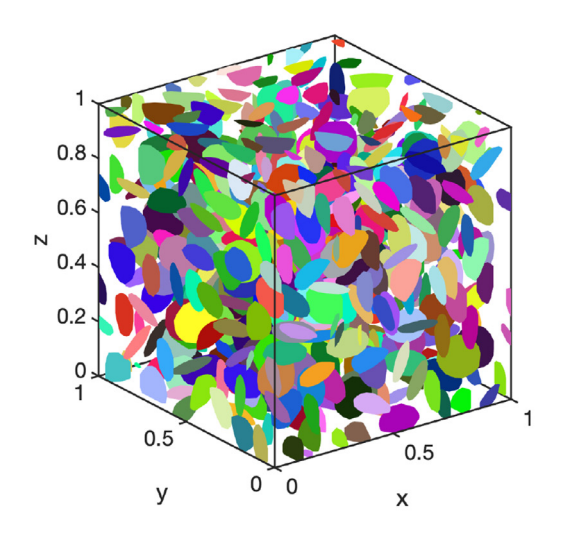
The stiffness matrix is close to isotropic because of the cumulative effect from the grains in random orientations. The isotropic stiffness and Poisson's ratio were approximated from the stiffness matrix and are shown.

A3. Case 2: Methodology using RVE of many particles

In this methodology, the effective stiffness was calculated using the RVE with 400 precipitates in random orientation. The effective stiffness matrix was calculated by applying a unit load in the RVE along the normal or shear directions. The obtained stiffness matrix



(a) Case 1: Multiscale modeling with 2 RVEs



(b) Case 2: RVE with random precipitates

Fig. A1. RVEs used for effective stiffness calculation in the two methodologies: (a) multiscale modeling with RVEs within grain and polycrystal, and (b) precipitates in a polycrystal matrix. The RVEs were constructed with a volume fraction of 20% and disc shaped precipitates of aspect ratio 4.

is the following.

$$\begin{bmatrix} C_{eff} \end{bmatrix} \approx \begin{bmatrix} 3.06 & 1.88 & 1.88 & 0 & 0 & 0 \\ 1.88 & 3.34 & 1.89 & 0 & 0 & 0.01 \\ 1.88 & 1.89 & 3.33 & 0 & 0 & 0 \\ 0 & 0 & 0 & 0.73 & 0 & 0 \\ 0 & 0 & 0 & 0 & 0.64 & 0 \\ 0 & 0.01 & 0 & 0 & 0 & 0.65 \end{bmatrix} GPa$$

$$\approx C[E = 1.85 \text{ GPa}, \ \nu = 0.37]$$

The stiffness matrix is close to isotropic from the cumulative effect of many random precipitates. The isotropic stiffness and Poisson's ratio were approximated from the stiffness matrix and are shown.

A4. Summary

The effective stiffness value from the case 1 and case 2 methodologies were calculated as 1.93 GPa and 1.85 GPa respectively. Although the precipitates were chosen with 100 times stiffer than the SMA matrix, the values obtained were of the same order as the SMA matrix (1 GPa). The values from the two methodology are

close within 5% absolute error. The close prediction from both the analysis indicate the methodology using many random precipitates in a polycrystal matrix can simulate the effective precipitated polycrystal SMA response within an accepted error.

Supplementary material

Supplementary material associated with this article can be found, in the online version, at doi:10.1016/j.actamat.2022.117929.

References

- D.C. Lagoudas, Shape Memory Alloys: Modeling and Engineering Applications, Springer, 2008.
- [2] O. Benafan, J. Brown, F. Calkins, P. Kumar, A. Stebner, T. Turner, R. Vaidyanathan, J. Webster, M. Young, Shape memory alloy actuator design: casmart collaborative best practices and case studies, Int. J. Mech. Mater. Des. 10 (1) (2014) 1–42.
- [3] J.M. Jani, M. Leary, A. Subic, M.A. Gibson, A review of shape memory alloy research, applications and opportunities, Materials & Design (1980–2015) 56 (2014) 1078–1113.
- [4] D.J. Hartl, D.C. Lagoudas, Aerospace applications of shape memory alloys, Proceedings of the Institution of Mechanical Engineers, Part G: Journal of Aerospace Engineering 221 (4) (2007) 535–552.
- [5] F.T. Calkins, J.H. Mabe, Shape memory alloy based morphing aerostructures, J. Mech. Des. 132 (11) (2010).
- [6] E.A.P. Hernandez, D.J. Hartl, D.C. Lagoudas, Active Origami: Modeling, Design, and Applications, Springer, 2018.
- [7] H. Stroud, D.J. Hartl, Shape memory alloy torsional actuators: a review of applications, experimental investigations, modeling, and design, Smart Mater. Struct. (2020).
- [8] A.A. Karakalas, T.T. Machairas, D.C. Lagoudas, D.A. Saravanos, Design of morphing strips using sma actuators under partial phase transformation operation, Smart Materials, Adaptive Structures and Intelligent Systems, volume 84027, American Society of Mechanical Engineers, 2020. V001T04A021
- [9] O. Ozbulut, S. Hurlebaus, R. Desroches, Seismic response control using shape memory alloys: a review, J. Intell. Mate.r Syst. Struct. 22 (14) (2011) 1531–1549.
- [10] G. Song, N. Ma, H.-N. Li, Applications of shape memory alloys in civil structures, Eng. Struct. 28 (9) (2006) 1266–1274.
- [11] J. Dong, C. Cai, A.M. Okeil, Overview of potential and existing applications of shape memory alloys in bridges, J. Bridge Eng. 16 (2) (2011) 305–315.
- [12] T. Duerig, A. Pelton, D. Stöckel, An overview of nitinol medical applications, Materials Science and Engineering: A 273 (1999) 149–160.
- [13] N. Morgan, Medical shape memory alloy applications the market and its products, Mater. Sci. and Eng.: A 378 (1-2) (2004) 16-23.
- [14] L. Machado, M. Savi, Medical applications of shape memory alloys, Brazilian journal of medical and biological research 36 (6) (2003) 683-691.
- [15] A. Bansiddhi, T. Sargeant, S.I. Stupp, D. Dunand, Porous niti for bone implants: a review, Acta Biomater. 4 (4) (2008) 773–782.
- [16] M.H. Elahinia, M. Hashemi, M. Tabesh, S.B. Bhaduri, Manufacturing and processing of niti implants: areview, Prog. Mater. Sci. 57 (5) (2012) 911–946.
- [17] J. Ma, I. Karaman, R. Noebe, High temperature shape memory alloys, Int. Mater. Rev. 55 (5) (2010) 257–315.
- [18] T. Umale, D. Salas, B. Tomes, R. Arroyave, I. Karaman, The effects of wide range of compositional changes on the martensitic transformation characteristics of nitihf shape memory alloys, Scr. Mater. 161 (2019) 78–83.
 [19] O. Benafan, G. Bigelow, D. Scheiman, Transformation behavior in niti-20hf
- [19] O. Benafan, G. Bigelow, D. Scheiman, Transformation behavior in niti-20hf shape memory alloys-transformation temperatures and hardness, Scr. Mater. 146 (2018) 251–254.
- [20] J. Ma, I. Karaman, R.D. Noebe, High temperature shape memory alloys, Int. Mater. Rev. 55 (5) (2010) 257–315.
- [21] H. Karaca, E. Acar, H. Tobe, S. Saghaian, Nitihf-based shape memory alloys, Mater. Sci. Technol. 30 (13) (2014) 1530–1544.
- [22] S. Besseghini, E. Villa, A. Tuissi, Ni□ ti□ hf shape memory alloy: effect of aging and thermal cycling, Materials Science and Engineering: A 273 (1999) 390–394.
- [23] I.D.N. AbuJudom, P.E. Thoma, M.-Y. Kao, D.R. Angst, High transformation temperature shape memory alloy, 1992, (????). US Patent 5,114,504.
- [24] H.E. Karaca, S.M. Saghaian, G. Ded, H. Tobe, B. Basaran, H.J. Maier, R.D. Noebe, Y.I. Chumlyakov, Effects of nanoprecipitation on the shape memory and material properties of an ni-rich nitihf high temperature shape memory alloy, Acta Mater. 61 (19) (2013) 7422–7431, doi:10.1016/j.actamat.2013.08.048.
- [25] A.A. Karakalas, D.C. Lagoudas, Preliminary design and numerical investigation of sma torsion tubes for the actuation of articulated adaptive panels, in: AIAA Scitech 2021 Forum, 2021, p. 1318.
- [26] J.H. Mabe, D.J. Hartl, N. Tichenor, M. Zackery, E. Blades, M. Nucci, Fluid-structure interaction modeling of a shape-memory alloy actuated supersonic wind tunnel model alloy, in: AIAA Scitech 2019 Forum, 2019, p. 0602.
- [27] J. Mabe, S. Frederes, D. Hartl, F. Carpenter, A direct comparison of shape memory alloy and electromechanical actuation for wing twist applications, in: Behavior and Mechanics of Multifunctional Materials IX, volume 11377, International Society for Optics and Photonics, 2020, p. 113770L.

- [28] F. Yang, D.R. Coughlin, P.J. Phillips, L. Yang, A. Devaraj, L. Kovarik, R.D. Noebe, M.J. Mills, Structure analysis of a precipitate phase in an ni-rich hightemperature nitihf shape memory alloy, Acta Mater. 61 (9) (2013) 3335–3346, doi:10.1016/j.actamat.2013.02.023.
- [29] A. Evirgen, I. Karaman, R. Santamarta, J. Pons, R.D. Noebe, Microstructural characterization and shape memory characteristics of the Ni50.3Ti34.7Hf15 shape memory alloy, Acta Mater. 83 (2015) 48–60, doi:10.1016/j.actamat.2014.09.027.
- [30] G. Bigelow, A. Garg, S. Padula Ii, D. Gaydosh, R. Noebe, Load-biased shape-memory and superelastic properties of a precipitation strengthened high-temperature ni50. 3ti29. 7hf20 alloy, Scr. Mater. 64 (8) (2011) 725–728.
- [31] A. Evirgen, F. Basner, I. Karaman, R.D. Noebe, J. Pons, R. Santamarta, Effect of aging on the martensitic transformation characteristics of a ni-rich nitihf high temperature shape memory alloy, Functional Materials Letters 5 (04) (2012) 1250038.
- [32] T. Yu, Y. Gao, L. Casalena, P. Anderson, M. Mills, Y. Wang, H-Phase precipitation and its effects on martensitic transformation in niti-hf high-temperature shape memory alloys, Acta Mater. 208 (2021) 116651.
- [33] O. Karakoc, C. Hayrettin, A. Evirgen, R. Santamarta, D. Canadinc, R. Wheeler, S. Wang, D. Lagoudas, I. Karaman, Role of microstructure on the actuation fatigue performance of ni-rich nitihf high temperature shape memory alloys, Acta Mater. 175 (2019) 107–120.
- [34] Z. Lu, G. Weng, Martensitic transformation and stress-strain relations of shapememory alloys, J. Mech. Phys. Solids 45 (11–12) (1997) 1905–1928, doi:10.1016/ S0022-5096(97)00022-7.
- [35] Z. Lu, G. Weng, A self-consistent model for the stress-strain behavior of shape-memory alloy polycrystals, Acta Mater. 46 (15) (1998) 5423-5433.
- [36] C. Collard, T. Ben Zineb, Simulation of the effect of elastic precipitates in SMA materials based on a micromechanical model, Composites Part B: Engineering 43 (6) (2012) 2560–2576, doi:10.1016/j.compositesb.2012.03.015.
- [37] C. Collard, T. Ben Zineb, E. Patoor, M.O. Ben Salah, Micromechanical analysis of precipitate effects on shape memory alloys behaviour, Mater. Sci. Eng., A 481–482 (1–2C) (2008) 366–370, doi:10.1016/j.msea.2007.05.112.
- [38] J.G. Boyd, D.C. Lagoudas, Thermomechanical response of shape memory composites, J. Intell. Mater. Syst. Struct. 5 (May) (1994) 333–346.
- [39] J.G. Boyd, D.C. Lagoudas, A thermodynamical constitutive model for shape memory materials. part ii. the sma composite material, Int. J. Plast. 12 (7) (1996) 843–873.
- [40] V. Birman, Properties and response of composite material with spheroidal superelastic shape memory alloy inclusions subject to three-dimensional stress state, J. Phys. D: Appl. Phys. 43 (22) (2010) 225402–225405, doi:10.1088/0022-3727/43/22/225402.
- [41] T. Baxevanis, A. Cox, D.C. Lagoudas, Micromechanics of precipitated near-equiatomic Ni-rich NiTi shape memory alloys, Acta Mech. 225 (4–5) (2014) 1167–1185, doi:10.1007/s00707-013-1071-3.
- [42] A. Cox, B. Franco, S. Wang, T. Baxevanis, I. Karaman, D. Lagoudas, Predictive modeling of the constitutive response of precipitation hardened ni-rich niti, Shape Memory and Superelasticity 3 (1) (2017) 9–23.
- [43] T. Baxevanis, A. Solomou, I. Karaman, D.C. Lagoudas, Full-Field Micromechanics of Precipitated Shape Memory Alloys, Springer International Publishing, Cham, 2018, pp. 225–255.
- [44] A. Solomou, G. Zhao, S. Boluki, J.K. Joy, X. Qian, I. Karaman, R. Arróyave, D.C. Lagoudas, Multi-objective bayesian materials discovery: application on the discovery of precipitation strengthened niti shape memory alloys through micromechanical modeling, Mater. & Design 160 (2018) 810–827.
- [45] J. Joy, A. Solomou, T. Baxevanis, D. Lagoudas, Predicting the constitutive response of precipitation hardened NiTiHf, Proceedings of SPIE The International Society for Optical Engineering 10165 (2017) 101650F.
- [46] D. Lagoudas, D. Hartl, Y. Chemisky, L. MacHado, P. Popov, Constitutive model for the numerical analysis of phase transformation in polycrystalline shape memory alloys, Int. J. Plast. 32–33 (2012) 155–183, doi:10.1016/j.ijplas.2011.10. 009.
- [47] L. Casalena, J. Sosa, D. Coughlin, F. Yang, X. Chen, H. Paranjape, Y. Gao, R. Noebe, G. Bigelow, D. Gaydosh, et al., Revealing transformation and deformation mechanisms in nitihf and nitiau high temperature shape memory alloys through microstructural investigations, Microsc. Microanal. 22 (S3) (2016) 1954–1955
- [48] A. Evirgen, Microstructural characterization and shape memory response of Ni-rich NiTiHf and NiTiZr high temperature shape memory alloys, 2014 Ph.D. thesis.
- [49] Tomviz software for tomographic visualization of 3D scientific data, http:// www.tomviz.org/.

- [50] B.D. Levin, Y. Jiang, E. Padgett, S. Waldon, C. Quammen, C. Harris, U. Ayachit, M. Hanwell, P. Ercius, D.A. Muller, et al., Tutorial on the visualization of volumetric data using tomviz, Micros. Today 26 (1) (2018) 12–17.
- [51] J. Ahrens, B. Geveci, C. Law, Paraview: an end-user tool for large data visualization, The visualization handbook 717 (2005).
- [52] S. Cao, M. Nishida, D. Schryvers, Quantitative three-dimensional analysis of ni4ti3 precipitate morphology and distribution in polycrystalline ni-ti, Acta Mater. 59 (4) (2011) 1780-1789.
- [53] R. Santamarta, R. Arróyave, J. Pons, A. Evirgen, I. Karaman, H.E. Karaca, R.D. Noebe, TEM Study of structural and microstructural characteristics of a precipitate phase in Ni-rich Ni-Ti-Hf and Ni-Ti-Zr shape memory alloys, Acta Mater. 61 (16) (2013) 6191–6206, doi:10.1016/j.actamat.2013.06.057.
- [54] MATLAB, Version 9.7.0 (R2019b), The MathWorks Inc., Natick, Massachusetts, 2019
- [55] G.S. Bigelow, A. Garg, S.A. Padula, D.J. Gaydosh, R.D. Noebe, Load-biased shapememory and superelastic properties of a precipitation strengthened hightemperature Ni 50.3Ti 29.7Hf 20 alloy, Scr. Mater. 64 (8) (2011) 725–728, doi:10.1016/j.scriptamat.2010.12.028.
- [56] B.C. Hornbuckle, T.T. Sasaki, G.S. Bigelow, R.D. Noebe, M.L. Weaver, G.B. Thompson, Structure-property relationships in a precipitation strengthened Ni-29.7Ti-20Hf (at%) shape memory alloy, Mater. Sci. Eng., A 637 (2015) 63–69, doi:10.1016/j.msea.2015.03.123.
- [57] D. Stroz, J. Kwarciak, H. Morawiec, Effect of ageing on martensitic transformation in niti shape memory alloy, J. Mater. Sci. 23 (11) (1988) 4127–4131.
- [58] I. Kaya, H. Karaca, M. Nagasako, R. Kainuma, Effects of aging temperature and aging time on the mechanism of martensitic transformation in nickel-rich niti shape memory alloys, Mater. Charact. 159 (2020) 110034.
- [59] J. Kim, S. Miyazaki, Effect of nano-scaled precipitates on shape memory behavior of ti-50.9 at.% ni alloy, Acta Mater. 53 (17) (2005) 4545–4554.
- [60] R. Hamilton, H. Sehitoglu, Y. Chumlyakov, H. Maier, Stress dependence of the hysteresis in single crystal niti alloys, Acta Mater. 52 (11) (2004) 3383–3402.
- [61] Y. Tong, F. Chen, B. Tian, L. Li, Y. Zheng, Microstructure and martensitic transformation of Ti49Ni51 xhfx high temperature shape memory alloys, Mater. Lett. 63 (21) (2009) 1869–1871, doi:10.1016/j.matlet.2009.05.069.
- [62] L. Bataillard, J.-E. Bidaux, R. Gotthardt, Interaction between microstructure and multiple-step transformation in binary NiTi alloys using in-situ transmission electron microscopy observations, Philos. Mag. A 78 (2) (1998) 327–344, doi:10.1080/01418619808241907.
- [63] E. Hornbogen, The effect of variables on martensitic transformation temperatures, Acta Metall. 33 (4) (1985) 595–601.
- [64] M. Smith, ABAQUS/Standard User's Manual, Version 6.9, Dassault Systèmes Simulia Corp, United States, 2009.
- [65] N. Zhou, C. Shen, M.-X. Wagner, G. Eggeler, M. Mills, Y. Wang, Effect of ni4ti3 precipitation on martensitic transformation in ti-ni, Acta Mater. 58 (20) (2010) 6685–6694.
- [66] J. Frenzel, E.P. George, A. Dlouhy, C. Somsen, M.-X. Wagner, G. Eggeler, Influence of ni on martensitic phase transformations in niti shape memory alloys, Acta Mater. 58 (9) (2010) 3444–3458.
- [67] O. Gal, fit_ellipse, MATLAB Central File Exchange, 2021. https://www.mathworks.com/matlabcentral/fileexchange/3215-fit_ellipse.
- [68] J. Michutta, M. Carroll, A. Yawny, C. Somsen, K. Neuking, G. Eggeler, Martensitic phase transformation in ni-rich niti single crystals with one family of ni4ti3 precipitates, Mater. Sci. and Eng.: A 378 (1–2) (2004) 152–156.
- [69] J. Michutta, C. Somsen, A. Yawny, A. Dlouhy, G. Eggeler, Elementary martensitic transformation processes in ni-rich niti single crystals with ni4ti3 precipitates, Acta Mater. 54 (13) (2006) 3525–3542.
- [70] O. Benafan, G. Bigelow, A. Garg, R. Noebe, D. Gaydosh, R. Rogers, Processing and scalability of nitihf high-temperature shape memory alloys, Shape Memory and Superelasticity 7 (1) (2021) 109–165.
- [71] H. Sehitoglu, Y. Wu, L. Patriarca, G. Li, A. Ojha, S. Zhang, Y. Chumlyakov, M. Nishida, Superelasticity and shape memory behavior of nitihf alloys, Shape Memory and Superelasticity 3 (2) (2017) 168–187.
- [72] P. Honarmandi, A. Solomou, R. Arroyave, D. Lagoudas, Uncertainty quantification of the parameters and predictions of a phenomenological constitutive model for thermally induced phase transformation in Ni–Ti shape memory alloys, Modell. Simul. Mater. Sci. Eng. 27 (3) (2019) 034001.
- [73] A. Cruzado, J. Segurado, D.J. Hartl, A.A. Benzerga, A variational fast fourier transform method for phase-transforming materials, Modell. Simul. Mater. Sci. Eng. (2021).